AN ABSTRACT OF THE THESIS OF

Matthew R. Leyden for the degree of Doctor of Philosophy in Physics presented on May 20, 2011

LABEL FREE BIOSENSING WITH CARBON NANOTUBE TRANSISTORS

Ethan D. Minot

As electronics reach nanometer size scales, new avenues of integrating biology and electronics become available. For example, nanoscale field-effect transistors have been integrated with single neurons to detect neural activity. Researchers have also used nanoscale materials to build electronic ears and noses. Another exciting development is the use of nanoscale biosensors for the point-of-care detection of disease biomarkers.

This thesis addresses many issues that are relevant for electrical sensing applications in biological environments. As an experimental platform we have used carbon nanotube field-effect transistors for the detection of biological proteins. Using this experimental platform we have probed many of properties that control sensor function, such as surface potentials, the response of field effect transistors to absorbed material, and the mass transport of proteins. Field effect transistor biosensors are a topic of active research, and were first demonstrated in 1962. Despite decades of research, the mass transport of proteins onto a sensor surface has not been quantified experimentally, and

theoretical modeling has not been reconciled with some notable experiments. Protein transport is an important issue because signals from low analyte concentrations can take hours to develop. Guided by mass transport modeling we modified our sensors to demonstrate a 2.5 fold improvement in sensor response time. It is easy to imagine a 25 fold improvement in sensor response time using more advanced existing fabrication techniques. This improvement would allow for the detection of low concentrations of analyte on the order of minutes instead of hours, and will open the door point-of-care biosensors.

LABEL FREE BIOSENSING WITH CARBON NANOTUBE TRANSISTORS

by

Matthew R. Leyden

A THESIS

submitted to

Oregon State University

in partial fulfillment of

the requirements for the

degree of

Doctor of Philosphy

Presented Defense May 20, 2011

Commencement June 2011

Doctor of Philosophy thesis of Matthew R. Leyden presented of May 20, 2011

Approved:

Major Professor, representing Physics

Chair of the Department of Physics

Dean of the Graduate School

I understand that my thesis will be a part of the permanent collection of Oregon State University Libraries. My signature below authorizes release of my thesis to any reader upon request.

Matthew R. Leyden, Author

ACKNOWLEDGEMENTS

Thank you Ethan, you have always been available to provide timely guidance and correction. Thank you Tristan, Landon, Tal for being available to discuss ideas and understanding and for providing entertaining conversation. I want to thank Canan for being a badass, and for being genuinely concerned about the progress of my research. Thank you members of the Minot group, past and present (Josh, Tom, Jenna, Jeff, Rachel, Daniel, Caleb,Micheal, Colin, Ramsi, and Jorg) for your contribution to my work.

I would like thank John wager for letting our group use his clean room, and Chris Tasker and Rick Presley for their help. Vince Remcho, and the members of your group (Myra Koesdjojo, Esha Chatterjee, Adeniyi Adenugaa) have been very helpful with PDMS, fluorescent microscopy, and understanding chemistry. Thank you Joe McGuire, and Karl (Rat) Schilke for your help with ellipsometry and surface chemistry. Thank you Janet Tate, for allowing us to use your thermal evaporator and for guiding me through graduate school. Thank you Paul Schule of Sharp labs for your many metal evaporations and for useful discussions. I would like to thank God and all of my friends that made life bearable during the hard times.

TABLE OF CONTENTS

TABLE OF CONTENTS (continued)

Page

TABLE OF CONTENTS (continued)

Page

List of Figures

List of Figures (continued)

Page

List of Figures (continued)

Page

List of Table

CHAPTER 1

INTRODUCTION

This chapter reviews existing biosensor techniques and explains how they work and how they are relevant. We expand on the topic of carbon nanotube field effect transistor biosensors and suggest that they have the potential to fill the unoccupied niche for low concentration point of care detectors.

1.1 Motivation for Biosensors

Biosensors are devices that detect the presence of specific biological molecules. In order to illustrate why detection of biological molecules is important consider the example of prostate cancer. With any cancer the odds of survival increase with earlier detection. The molecule prostate specific antigen (PSA) exists in a man's blood at low levels when he is healthy, but will usually be in abundance when he has prostate cancer. The background level of PSA is about 10 pM.[1] If a sensor is able to detect PSA at concentrations of 10 pM and above the sensor could potentially recognize the cancer right after it develops, which enables the highest possible odds of survival.

There are many examples of biomarker molecules similar to PSA that we might want to detect, such as human chorionic gonadotropin, which is detected in home pregnancy tests, and glucose, where concentration is measured daily for diabetics. Biosensors can also be made to recognize DNA,[2] which is useful for the detection of genetic diseases. This work focuses on using carbon nanotube field-effect transistors (CNT FET) as biosensors and explains how CNT FETs can be used to detect biological

molecules. Carbon Nanotubes are smaller than any other field-effect transistor, they are potentially cheap to manufacture, and respond faster than required for absorption experiments.

Beyond detecting the presence of an antigen, biosensors can also be useful in learning about binding kinetics and enzyme reaction rates.[3] Kinetics experiments need measurements on the time scale of the event. Proteins binding to a sensor can take minutes to hours depending on concentrations. So measurement techniques that update every second or faster are desirable. Label-based techniques such as a fluorescent sandwich assays, or magnetic bead assays do not measure the protein directly and are not appropriate for measuring protein kinetics. These label-based techniques are sensitive to the kinetics of tag attachment and not the kinetics of protein binding. Carbon nanotube FETs have the potential to measure protein kinetics because they sense the protein directly and offer high temporal resolution.[4,5]

Another desirable feature of a biosensor is point-of-care use, where the measurement device is taken to the patient, rather than sending samples to a lab. This style of sensor must be easy to use and inexpensive. An example of a successful electronic-based point-of-care biosensor is the at-home glucose blood meter. The initial equipment is purchased with less than $100 and the disposable sensor coupons cost less than $1 each. They are simple to use and require no special training. Nanoscale FET sensors have already been shown effective when using whole blood,[6] and are showing promise for use as point-of-care sensors.

1.2 Biosensing Techniques

There are a number of existing methods for biosensing. Some commercially available examples include enzyme-linked immunosorbent assays (ELISA), DNA chip assays,[2] and surface Plasmon resonance.[3,7] Some technologies that are in development are silicon nanowire sensors,[8] magnetic bead sensors,[9] graphene sensors,[10] and CNT sensors.[11] All of these techniques can be classified into one of two categories, label-based sensing and label-free sensing. A label-based technique uses a label that can be easily detected. For example ELISA and DNA chips require the attachment of fluorescent tags that are easily seen when viewed with a fluorescent microscope. Magnetic bead sensors use a magnetic bead as the tag, and the change in magnetic field is detected by the sensor. Label-free techniques require no label and detect the presence of the molecule directly. Surface Plasmon resonance, silicon nanowires, and carbon nanotube transistors are all examples of label-free techniques. Carbon nanotube, graphene, and silicon nanowire transistors detect bound antigen by the change in local electric field. Label-free techniques remove the need for an intermediate tagging step.

All techniques rely on the use of antibodies or aptamers to capture biomarker proteins onto a surface. A diagram of an antibody is shown in Fig. 1.1.[12] The antibody will only bind to a specific molecule called an antigen. Antibodies are proteins created by the immune system of an organism. Antibodies can be collected from a living organism (rabbit for example) and are separated and concentrated for use in biosensor applications. A synthetic version of an antibody made from RNA or DNA is called an aptamer.[13,14]

Since aptamers are smaller and less complicated they are more stable and have a longer shelf life. [15] Aptamers are smaller than antibodies, which brings the antigens closer to a field-effect sensor, making them more effective for use in FET biosensors. More detailed information on aptamers can be found in section 5.1.

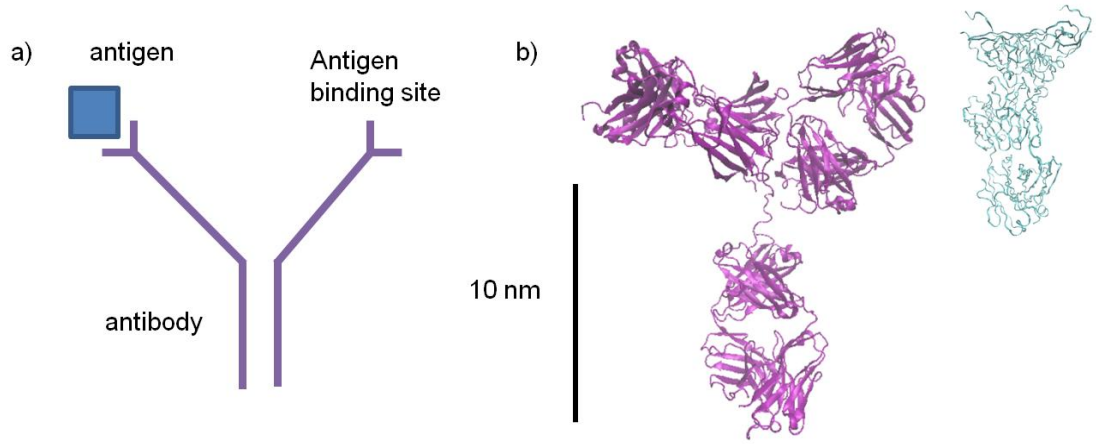

Fig. 1.1 Diagrams of an antibody. a) All antibodies have this characteristic Y shape in their structure. The ends of the Y at the top function as the antigen binding site, where only specific molecules bind. The size of a typical antibody is around 10 nm in length. b) Crystal structure of IgG specific to HIV virus determined by x-ray crystallography,[12] next to a small section of the HIV virus, the CD4 binding site where the antibody binds.[16]

1.2.1 Fluorescent Immunoassays (established label-based technique)

A Fluorescent immunoassay is a technique where a fluorescent tag is used to identify the presence of a protein in solution. [2,17] An example of this technique is the fluorescent sandwich assay. A surface is covered with an array of antibodies, where each point of the array will detect the presence of a specific antigen. The surface is then treated with a sample solution, which may or may not contain the relevant antigens. The surface is rinsed and then treated with a solution of fluorescently tagged antibodies. If the

antigen is present, there will be a complete sandwich and the fluorescent tag will attach to the surface. The sample is analyzed with a fluorescent microscope to check for fluorescence, and therefore the presence of antigen. This procedure is shown in Fig. 1.2. The same procedure can be done with an enzyme tag (ELISA) instead of a fluorescent tag.

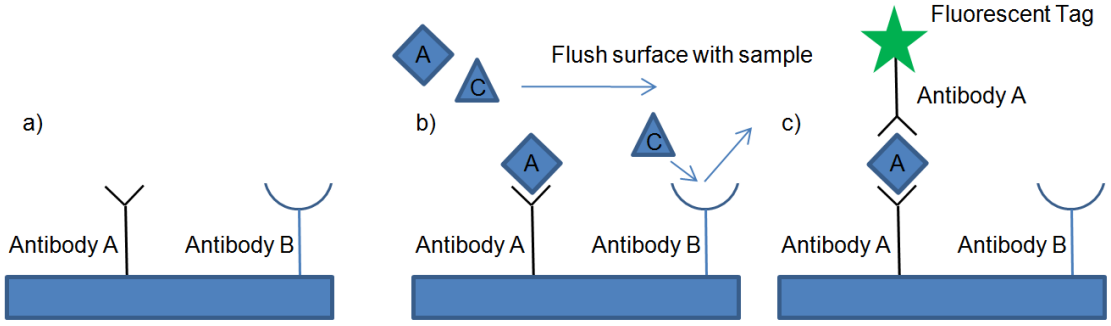

Fig. 1.2 Fluorescent sandwich assay a) Shows a surface that has been treated with two types of antibodies A, and B. These antibodies will bind to antigens A, and B respectively. b) If we flush the surface with a solution containing antigens A, and C, then there will only be binding between antigen A and antibody A. Antigen C and antibody B will not be able to form a conjugate pair. c) The surface is then flushed with a solution of fluorescently tagged antibodies A and B, but only A will bind because only antibody A has an antigen. The presence of antigen A in solution is then inferred from a fluorescence measurement.

Fluorescent microscopy and ELISA are widely used techniques that can be used to detect single molecules.[18] Despite being able to measure single molecules, fluorescent microscopy is still limited by the diffusion based capture of proteins. The process of detection has multiple steps and can take a long time for a result. Measurement is done after the addition of the tag and not when the protein binds and therefore will not be able to give information on protein kinetics. Fluorescent microscopy requires expensive equipment and a trained operator, which prohibits point-of-care detection.

1.2.2 Surface Plasmon Resonance (established label-free technique)

Surface plasmon resonance (SPR) is an optical technique used for biosensing.[3] Plasmons are optical waves that propagate along the surface of a metal. These waves interact with adsorbed material near the metal surface. The coupling between a free-space light wave and the plasmon mode is very sensitive to absorbed material. The reflected light intensity changes when the plasmon coupling changes. This process is shown in Fig. 1.3. This technology is commercially available and can be bought through Biacore.[7]

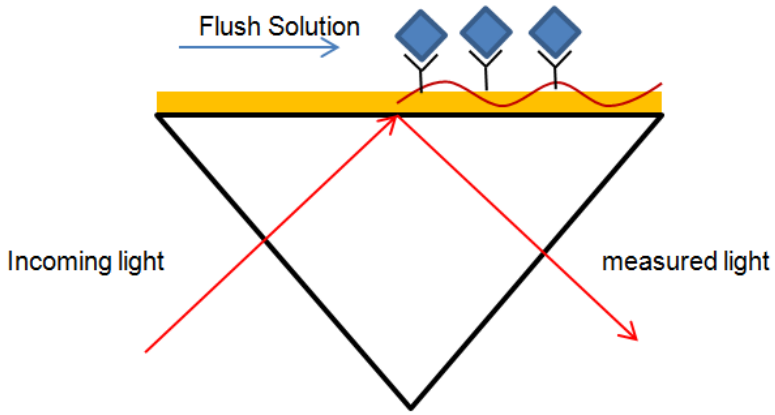

Fig. 1.3 Surface Plasmon resonance. Light shines through a prism and reflects off the thin metal surface, some of the light couples to the surface plasmon mode. The optical waves at the surface of the metal are the surface plasmons. Antigens that have bound to the surface change the properties of the surface plasmons and therefore change the reflected light.

This is an effective technology and can easily detect nanomolar antigen concentration.[7] Measurements are taken on the time scale of protein absorption, which allows for protein kinetics measurements. The main limitation of a surface Plasmon resonance biosensor is that it requires expensive equipment and is only appropriate for lab applications.

1.2.3 Field-Effect Transistor Sensors (technique under development)

There are many techniques in development that use field-effect transistors to detect the presence of an antigen. Some examples include field-effect transistors made from carbon nanotubes,[19,20,21] silicon nanowires, [8,22] silicon on insulator wafers (SOI),[6,23] and graphene.[10,24] All of these materials respond by the same basic detection mechanism.

Sensors made from these novel materials are on the nanoscale and are therefore sensitive to low concentrations of analyte. Nanowire biosensors are reported to detect femto-molar concentrations[25]. Silicon on insulators have been shown to detect nanomolar concentrations.[23] Graphene biosensors have reported to detect 10 picomolar concentrations.[24] Carbon nanotubes biosensors have been shown to detect in hundreds of picomolar concentrations,[26] and are explained in greater detail in section 1.4.

Field-effect transistors (FET) change conductance when there is a change in the local electrostatic potential. For example a protein that absorbs onto the FET will introduce a new distribution of charge, causing a change in conductance. The surface of these FET materials can be functionalized with antibodies and the transistor can be used as an antigen specific biosensor. A schematic of a generalized FET biosensor is shown in Fig. 1.4a. Cross sections of FET channels made from silicon nanowires, CNTs, graphene and SOI wafers are shown in Fig. 1.4b,c,d and e and are drawn to approximate scale.

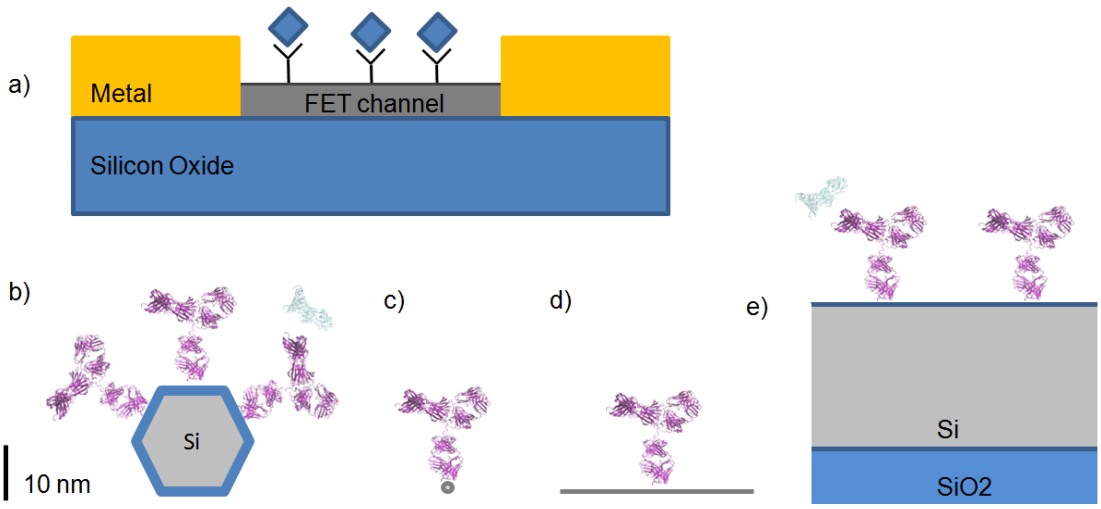

Fig. 1.4 Field effect transistor biosensors a) Schematic of a field effect transistor biosensor functionalized with antibodies. b-e)Approximate scale of 4 types of field effect transistors functionalized with and antibody b) Silicon nanowire (~20 nm), with a 2nm native silicon oxide c) Carbon nanotube (~2 nm) d) graphene (~1 nm) e) Silicon on insulator FET where silicon is about 25 nm thick.

Field-effect transistors have high temporal resolution so they have potential to be used in the study of protein kinetics. Field-effect transistors use electrical based detection. Like other electronics they can be made small, cheap, and simple to use, allowing them to be used for point-of-care applications.

One issue with all FET sensors is that they are limited by the screening length in solution (more in chapter 2). A FET can only detect things a very short distance away. In biological conditions the screening length (1 nm) is shorter than the size of an antibody (10 nm). This means that the signal generated when an antigen binds to an antibody will be too small in biological conditions and will not be detected by the sensor. There are various ways around this issue. For example, by bringing the protein closer to the sensor

by using aptamers the FET has a larger signal.[26] Also, it is possible to increase the screening length with lower salt concentration, which allows for detection at greater distances. [25,27]

One challenge still being overcome is that CNT and nanowire growth produces materials with a distribution of electrical characteristics. This makes it difficult to fabricate consistent FET sensor devices. There are techniques used to selectively separate,[28]or selectively grow particular CNT chiralities.[29] Solutions of separated tubes can be commercially purchased through Nanointegris.

Biosensors are an important tool used for early disease detection, and for gaining a greater understanding of proteins. Carbon nanotube transistor biosensors have potential to satisfy the need for low limits of detection, point-of-care applications and measure protein binding kinetics.

1.3 Carbon Nanotubes in General

Nanotubes have many exciting properties like their high tensile strength, high carrier mobility, small dimensions, and FET behavior. This work is interested in the last three properties, the small size and high sensitivity to electric fields is very useful for detection and the high carrier mobility is important to measure fast protein kinetics.

Carbon nanotubes (CNTs) have many useful properties that have made them the topic of research in many areas. They were first discovered and popularized by Iijima in 1991.[30] Some notable examples of the properties of nanotubes are that they have a very high tensile strength.[31,32] This high tensile strength makes them an exciting light weight,

high strength material. Carbon based semiconducting materials such as CNTs[4] and graphene[33] have very high carrier mobility. Therefore CNTs have potential for use in nanoscale high speed electronics.[5] They have a high surface area to volume ratio, which makes them good biosensors.

Carbon nanotubes are molecules of carbon that form a hollow tube. This can be thought of as a sheet of graphene rolled up into a tube. A diagram of a CNT is shown in Fig. 1.5 The diameter of the tube, and how it is rolled, can affect the electrical properties (more in chapter 2). How the sheet is rolled is defined by its chirality, or handedness of the CNT. For example a sheet of paper can be rolled so that the edges are parallel, or it can be rolled so the edge forms a spiral.

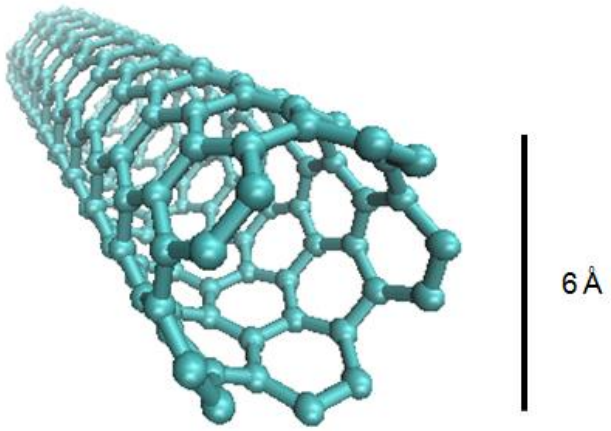

Fig. 1.5 Model of a (5,5) carbon nanotube rendered in VMD (free molecular visualization software)

Carbon nanotubes are made with a wide variety of processes, but all nanotube growth can be grouped into one of three following methods. Arc discharge was the first method used to produce CNTs[30]. They are made when a high current is run through

graphite electrodes. The high heat generated in the arc discharge creates carbon nanotubes. Laser ablation was next the method discovered for producing carbon nanotubes.[34] A pulsed laser shoots at a graphite target vaporizing the carbon. Nanotubes then condense on the cool nearby surfaces where the nanotubes are collected. Chemical vapor deposition is the most recent technique. [35] This technique is now widely used for commercial applications and produces high quality single walled carbon nanotubes (more information in chapter 3). This method uses a furnace to heat a CNT catalyst in the presence of a carbon source gas. Carbon nanotubes are then grown from the catalyst. These methods all produce a distribution of CNTs with different sizes and properties. Significant work has been put into selective growth of CNTs,[29] or separating out specific chiralities after growth.[28]

1.4 Carbon Nanotube Biosensors

Nanotube biosensors use the field-effect transistors properties of the nanotube to detect the presence of adsorbed biological molecules. A change in electric field generated by a bound molecule changes the effective gate voltage on the CNT and causes a change in conductance, as shown in Fig. 1.6. The protein does not need to have a net charge since there will still be non-zero electric fields when close to the protein (like a dipole). The bound protein can also change the coupling between the liquid gate and the CNT to generate a conductance change.[36,37] More detail on the electronic response of CNT FETs can be found in sections 2.4 and 5.2.

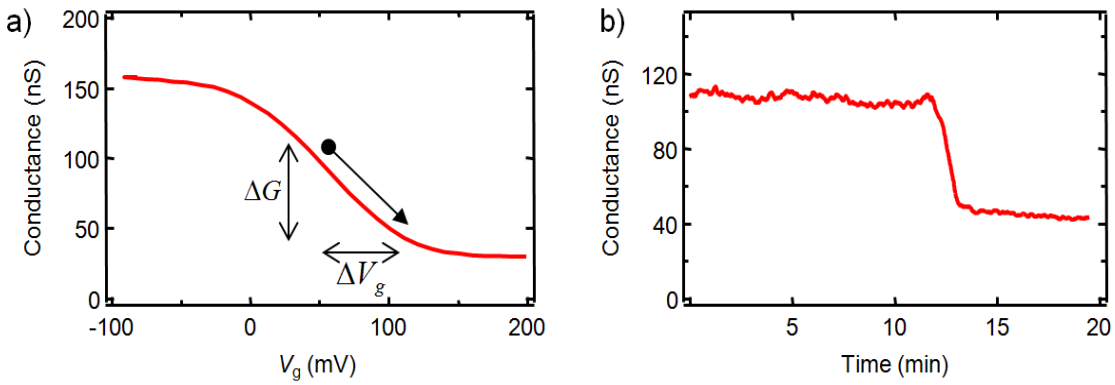

Figure 1.6 Typical Nanotube Biosensors a) Transistor curve of CNT in solution gated by a reference electrode. The changes in conductance and gate voltage ΔG and ΔV_g show how the curve changes after the addition of protein. V_g is set to 50mV b) The real time measurement of the adsorption of a 10 ug/ml poly lysine (MW110kD) solution at 33 μl/min

Carbon nanotube field-effect transistor (CNT FET) biosensors are made by connecting metal contacts to either side of a CNT. A source-drain voltage is applied to the metal to drive a current through the CNT. A gate voltage is applied to the CNT by back gating or by solution gating. The gate voltage controls the local field around the CNT and therefore its conductance. A diagram of a CNT circuit is shown in Fig. 1.7. More details about CNT FET fabrication and operation can be found in chapter 3.

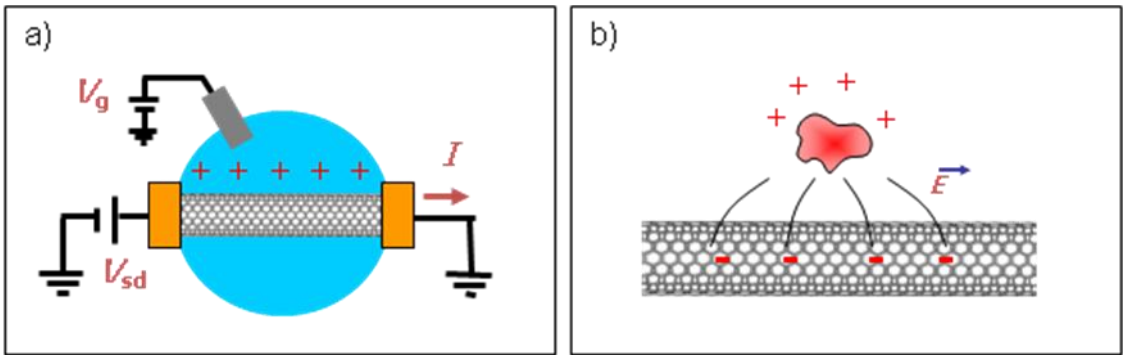

Fig. 1.7 Gating of CNT field effect transistors. a) This is a cartoon of a CNT transistor gated in solution by a Ag/AgCl electrode. Applied charge will induce a counter charge in the CNT that increases the number of current carriers b) This is a cartoon of a nanotube being gated by a charged protein.

Carbon nanotubes and graphene have the largest surface area to volume ratio of any semiconducting nanomaterial, and they have no inert oxide layer. These things make CNTs FETS a very promising choice for their use as biosensors.

Pioneering work demonstrated CNT biosensors the detection of glucose with glucose oxidase sensors[19] and streptavidin with biotin coated sensors [20]. There are a number of other published papers that have demonstrated functionalized nanotube biosensors. The following are a few examples demonstrating lower detection limits. Immunoglobulin E was detected at 250 pM concentrations using aptamers,[26] Pig serum albumin was detected at 5 nM concentrations,[38] and 10nM Thrombin was detected using aptamers.[39]

Several of these papers reporting low limits of detection use aptamers. Aptamers are shorter synthetic versions of antibodies.[13,14] The main advantage of the aptamer is that it is shorter and brings the antigen closer to the nanotube, and therefore generates a larger change in potential. Notice that none of the examples mentioned above had detected

concentrations at the background levels of our example of 10 pM PSA.[1] Therefore, there is still a clear need for improvement in CNT FET biosensors.

1.4.1 Protein Delivery in Biosensors

Protein transport is an important issue for biosensors. In the beginning of this chapter we set a low end limit concentration we would want to detect with a biosensor of 10 pm.[1] The flux of protein to a surface is linearly proportional to the initial concentration (more in chapter 4),[40] so lower concentrations will have lower protein flux and will take longer to generate a signal. Consider the example of 250 pM detection of imuno globulin E, which took approximately 25 min to detect,[26] and compare it to a hypothetical 10 pM concentration. It would take approximately 25 times longer to generate the same signal, which is over 10 hours. In order to make low concentration detection practical we need to either increase the signal-to-noise ratio of the sensor, or increase the flux of protein. A number of papers have addressed the issue of signal-to-noise,[37] but before this work no one has increased the protein flux, although the issue had been addressed theoretically.[41,42]

One way to increase the protein flux is to limit the available binding length to the proteins. By treating the inactive surfaces of the chip with a coating that proteins do not stick to, non-specific binding is limited. Therefore the concentration of protein is not depleted by nonspecific binding, and effectively increases the concentration seen by the sensor. Besides increasing the protein flux onto the sensor, non-stick coatings reduce the total amount of protein required to generate a signal. For example, it is desirable to draw

the minimum amount of blood from a patient and if the number of proteins necessary for detection is reduced so is the volume of blood required.

In chapter 4 we demonstrate a 2.6 fold increase in protein flux using the protein repellent coating polyethylene glycol. It is easy to imagine using modern submicron photolithography techniques to increase this factor to 25 allowing our IgG E detection example to have a 25 min binding time for the detection of 10 pM concentrations. In this way PEG treatments are a low hanging fruit to the improvements of biosensors.

1.5 Overview of Thesis

Chapter 2 examines the electron transport effects that are relevant to biosensor operation. A model is given for CNT conduction based on the Landauer-Buttiker formula and Schottky barrier contacts. In this model there are various ways a CNT biosensor will respond to absorbed protein. This chapter also discusses the role of the salt solution on the behavior of CNT biosensors and the importance of the Debye screening length. Carbon nanotubes are temperature dependent, especially when operated in the subthreshold regime, and we calculate the effects of a small temperature change on conductance.

Chapter 3 discusses the fabrication of CNT FETs and the experimental techniques we have employed for biosensor measurements. Some topics include the details of microfabrication such as photolithography, CNT growth by chemical vapor deposition, thermal evaporation of metal thin films. We also explain how electrical measurements of

the CNT circuits are made and how the CNT chip is integrated with a microfluidic system. The microfluidic delivery system is calibrated with pH sensing experiments.

Chapter 4 discusses the mass transport of proteins to a CNT FET biosensor. We show that the protein repellent coating polyethylene glycol (PEG) repels our model protein polylysine. We then pattern our sensors with PEG to limit the binding length and show that protein flux can be increased, therefore making a faster sensor. We do some first order calculations which show how much of improvement we can hope to expect by limiting the binding length as well as experimentally demonstrate a 2.6 fold improvement in response time.

Chapter 5 details experiments we have undertaken on various biologically relevant proteins. We demonstrated the detection of DNA and showed that it gave a response consistent with its negatively charged backbone. We then compare the DNA experiment to the positively charged polylysine and see a shift in gate voltage opposite of polylysine. We also discuss attempts to functionalize CNTs. We use the molecule 1-pyrenebutanoic acid succinimidyl ester which has a pyrene end that attaches to the nanotube and an ester end that will bind to an amine group on a protein.

CHAPTER 2

MODELING CARBON NANOTUBE TRANSISTORS

This chapter discusses the theory used to model the conductance of a CNT transistor operated in liquid environments. We model the CNT as a 1D conductor and use a modified version of the Landauer-Buttiker formula that includes effects of Schottky barrier tunneling. We then fit this model to our experimental data and find qualitative agreement. The potential at the sensor surface is modeled with Stern's theory. We present a derivation of the surface potential as a function of surface charge, and introduce the idea of screening length in solution. We show that experimentally observed changes in CNT electrostatic doping are in quantitative agreement with Stern theory and the surface charge of silicon oxide. We show that CNT FETs are sensitive to temperature when operated and in the subthreshold regime, which shows that care should be taken to control temperature during sensing experiments.

2.1 Bandgaps of Carbon Nanotubes

Carbon nanotubes can either be metallic or semiconducting depending on the diameter and chirality of the CNT. This work exclusively considers semiconducting CNTs because semiconducting CNTs are sensitive to charged proteins. An estimate of the band gap of a semiconducting CNT can be made based on the band structure of graphene.[43]

$$E_g \approx \hbar v_F \frac{4}{3d} = \frac{0.88eV \cdot nm}{d} \tag{2.1}$$

Where d is the diameter and we assume the Fermi velocity, v_F, is $1x10^6$ m/s. Equation 2.1 is relevant when we want grow CNTs with a particular band gap, and therefore particular diameter.

2.2 Stern Model for Surface Potential

In this section we develop the theory for the electrostatic potential in electrolyte solutions. The electrostatic potential tunes the conductivity of semiconducting CNTs and therefore is critical to understanding CNT FET biosensor operation.

The distribution of ions in a solution contacting a charged surface is described by the Stern model. There are two layers of ions in this model. The first layer is a compact layer of ions at the solid surface called the Helmholtz layer. The second is a diffusive layer of ions that sit above the Helmholtz layer. The characteristic length that electric fields penetrate ionic solutions is called the Debye screening length. The Debye screening length can be a limiting factor for FET biosensors since antibodies are longer than the Debye screening length in biological solutions. To resolve this limitation it is important to understand what controls the Debye screening length and the potential at the CNT sensor.

In the bulk of a salt solution there is a balance of positive and negative ions. If there is a charged surface present in the solution, ions of the opposite charge are attracted to the surface, screening the fixed charge. The higher the salt concentration the more effectively the surface will be screened. This situation is described by the Gouy-Chapman-Stern theory.[44,45] In this model the ionic charges in solution screen out the

charges on the surface in two ways as illustrated in Fig. 2.1.

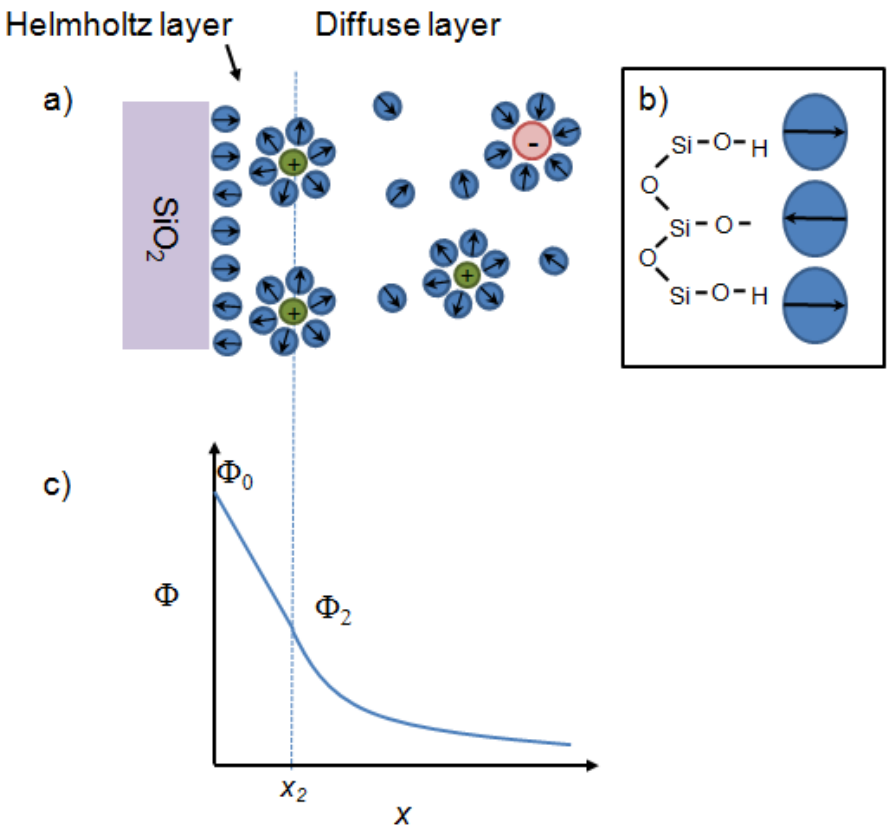

Fig. 2.1 Stern Model of surface potential. a) Cartoon of a charged surface in solution. Positive charges move towards the negative charges in the surface to form a compact layer of ions. There is a layer of water of water molecules (blue circles) that surrounds the ions and covers the surface. In the case of sodium ions attracted to a negatively charged surface the thickness of the Helmholtz layer will be around 0.7 nm. For positively charged surfaces chlorine is attracted. Chlorine is a larger ion and requires more energy for a hydration layer and will instead be indirect contact with a charged surface. Any screening not done in the Helmholtz layer is screened by the diffuse layer in solution. b) The water molecules at the silicon oxide surface orient their dipoles to facilitate hydrogen binding with the oxide c) Potential profile at the surface. The slope of the potential is linear within the Helmholtz layer, but is an exponential in the diffuse layer. A dashed line marks the transition between layers.

First, ions form a thin compact layer of counter charge called the Helmholtz layer. The thickness of this layer is defined by the size of the ions and the layer of water that

surrounds the ions and covers the surface. Compact layers of charge are entropically unfavorable and only form at higher ion concentration and at highly charged surfaces. The second layer of screening ions is called the diffuse layer. For the case of a typical ionic solution (10 mM NaCl) the drop in electrostatic potential across the diffuse layer can be up to 100mV. Any further drop in potential will occur across the Helmholtz layer.

There is no simple way of measuring the potential drop across the Helmholtz layer and the diffuse layer independently. However, there are techniques used for measuring both the Helmholtz and the diffuse potential together, this total drop in potential is called the zeta potential. The zeta potential will vary depending on surface charge density and salt concentration and will be equal to the sum of the Helmholtz potential and diffuse potential under no-slip flow conditions.

The total charge per unit volume ρ, in a solution at potential Φ, is given by the Boltzmann equation.[44]

$$\rho(x) = \sum_i n_i Z_i e \cdot \exp\left(\frac{-Z_i e\Phi(x)}{k_B T}\right) \tag{2. 8}$$

Where Φ is measured with respect to bulk solution, n is the bulk concentration of ions, Z is the charge of the ion, and e is the charge of an electron. The Poisson equation provides and an additional constraint on the relationship between ρ and Φ

$$\rho(x) = -\varepsilon\varepsilon_0 \frac{d^2\Phi(\mathrm{x})}{dx^2} = \sum_i n_i Z_i e \cdot \exp\left(\frac{-Z_i e\Phi(x)}{k_B T}\right). \tag{2.9}$$

The Poisson-Boltzman equation can be solved for the special case of monovalent symmetrical electrolytes (Example NaCl, Z:Z, Z=1).Where the constants ε and ε_0 are the relative permittivity of water (ε = 80) and vacuum permittivity.

$$\frac{d\Phi(x)}{dx} = -\left(\frac{8k_BTn}{\varepsilon\varepsilon_0}\right)^{1/2} \sinh\left(\frac{e\Phi(x)}{2k_BT}\right) \tag{2.10}$$

Equation 2.10 describes the distribution of ions of the diffuse layer above a charged surface. To find the potential in the diffuse region, we integrate Eqn. 2.10 to solve for Φ_0, the potential at solid surface, and the potential Φ_2, the potential at the start of the diffuse layer.

$$\int_{\Phi_2}^{\Phi} \sinh\left(\frac{e\Phi(x)}{2k_BT}\right)^{-1} d\Phi = -\left(\frac{8k_BTn}{\varepsilon\varepsilon_0}\right)^{1/2} \int_{x_2}^{x} dx \tag{2.11}$$

$$\frac{\tanh(e\Phi(x)/4k_BT)}{\tanh(e\Phi_2/4k_BT)} = \exp\left(\frac{-(x-x_2)}{\lambda}\right) \tag{2.12}$$

Where x_2 is the edge of the Helmholtz plane and λ is the Debye screening length

$$\lambda = \sqrt{\frac{\varepsilon\varepsilon_0 k_BT}{2nZ^2e^2}} \approx \frac{1\text{nm}}{\sqrt{c/93\text{mM}}}, \tag{2.13}$$

where *c* is the molar concentration. For many situations Eqn. 2.12 can be simplified as exponential model and the Helmholtz layer can be ignored giving

$$\Phi(x) = \Phi_2 e^{-x/\lambda}. \tag{2. 14}$$

Biological conditions are often used in our experiments. Phosphate buffered saline (PBS, 137 mM NaCl and 10mM $Na_3(PO_4)$) simulates the electrolyte concentrations

found in blood serum and inside cells. Phosphate buffered saline has a Debye screening length $\lambda \sim 1$ nm, therefore separation distances must be ~ 1 nm for optimal sensing.

It is important to know how much the potentials Φ_0 and Φ_2 change when charged proteins bind to a surface. The zero-order approximation is that the potential drop across the diffuse layer will not exceed 100 mV. We can look at Eqn. 2.12 and see that the relevant energies are on the order of $4k_BT$ or 100 mV. We estimate the thickness of the Helmholtz layer to be 700 pm (diameter of 2 water molecules and the radius of the ion, refer to Fig. 2.1) based on the average diameter of non-hydrated sodium (204 pm) and the diameter of a water molecule (290 pm). This is smaller than the diameter of a 1-3 nm CNT, which means the bulk of the nanotube resides in the diffuse layer. The average potential on the surface of the nanotube is controlled by the potential in the diffuse layer, and will not exceed the maximum of 100 mV.

Equation 2.15 gives a more quantitative relation between surface charge σ and the diffuse layer potential Φ_2.[44] This result is derived by using Gauss's law. The electric field is zero far into the solution at one side of a Gaussian box. The other end of the box at the surface, we can find the *E* field using Eqn. 2.10 (x=0). We assume there is no field through the sides of the box since the layer is uniform parallel to the surface.

$$\sigma = \sqrt{8k_{\mathrm{B}}T\varepsilon\varepsilon_0 n}\sinh\left(\frac{Ze\Phi_2}{2k_BT}\right) \tag{2.15}$$

We can use this equation to calculate $\Phi_2 = 28$ mV on a SiO_2 surface in a 100 mM salt solution, where the SiO_2 surface charge is roughly -2.5 μCcm^{-2}.[36] This surface charge

is equivalent to one electron per 2.5 x 2.5 nm square. From here we estimate the potential at the surface $\Phi_0(x=0)$ assuming a Helmholtz layer thickness of 7 angstroms and a uniform electric field within the plane of $\sigma/\varepsilon_r \varepsilon_0$.

$$\Phi_0 = \Phi_2 - \frac{d\Phi}{dx}_{x=x_2} x_2 \tag{2.16}$$

This gives a give a value $\Phi_0 = 53$ mV. This is equal to the zeta potential under no-slip conditions. Since $\Phi_0 = 53$ mV and $\Phi_2 = 28$ mV there is an 25 mV drop across Helmholtz layer.

The relationship between σ and Φ is useful for quantifying the capacitive coupling between an electrolyte solution and a surface. The differential capacitance C_d is defined as $d\sigma/d\Phi_0$, which is analogous to the familiar Q/V. The differential capacitance can be found by taking the derivative of Eqn. 2.15 and substituting Φ_2 from Eqn. 2.16. This capacitive coupling affects the performance of CNT FET biosensors.

$$\frac{1}{C_{dl}} = \frac{x_2}{\varepsilon\varepsilon_0} + \frac{\lambda}{\varepsilon\varepsilon_0 \cosh\left(\frac{Ze\Phi_2}{2k_B T}\right)} \tag{2.17}$$

This is analogous to two parallel plate capacitors in series, where one has a separation on the order of the Helmholtz layer thickness x_2 and the other has a separation equal to the Debye screening length λ. To get an order of magnitude estimate we ignore the potential dependence and assume that the cosh term is about 1 and get a double layer capacitance of about 0.4 F/m^2.

2.3 Carbon Nanotube Field-Effect Transistors (CNT FETs)

This work revolves around the carbon nanotube field-effect transistor (CNT FET) and it is important to understand how it functions. A FET is a current carrying device that is turned on or off by an applied electric field. In the case of the CNT FET, the current is carried by a 1D conductor with two factors controlling the resistance, the channel resistance and the contact resistance.

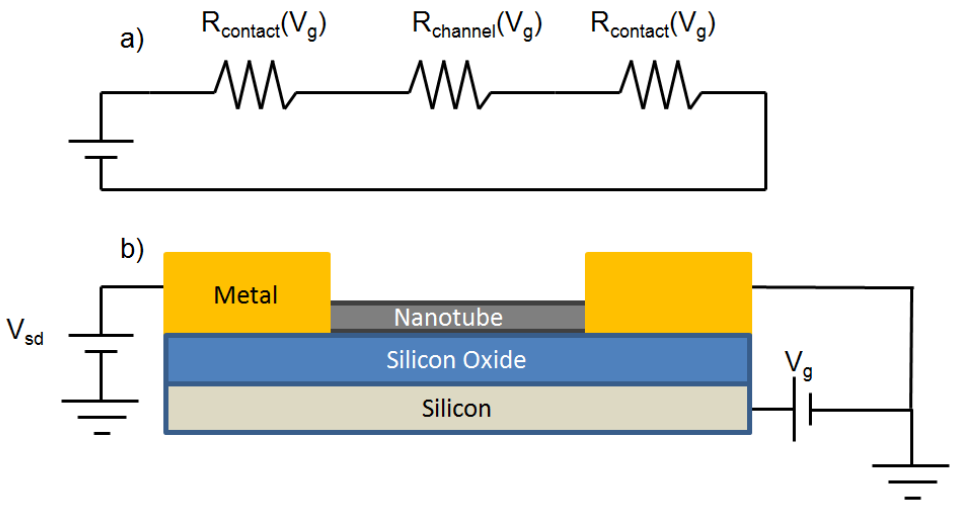

Fig. 2.2 Modeling a carbon nanotube field effect transistor. a) The equivalent circuit model has two sources of resistance, the contacts and the channel. Note that a CNT FET does not behave as a set of resistors in series, and this diagram is only used to illustrate circuit geometry b) Schematic of a nanotube circuit showing metal contacts and a nanotube on a silicon wafer. The contact resistance comes from the Schottky barrier at the nanotube metal interface.

There is a fundamental minimum resistance for a CNT device $R_{min} \approx$ 6.5 kΩ.[46] This minimum resistance is one fourth the quantum of resistance $R_Q = h/e^2 \approx 25.8$ kΩ. Carbon nanotube circuits only reach this minimum resistance limit in the ballistic regime, where carriers travel straight through the CNT without scattering. The scattering length

for CNTs is on the order of a few hundred nanometers at room temperature.[47] The CNT FETs in this work generally use nanotubes that are 4 μm long or longer and carriers will scatter many times while traveling through the tube. The resistance R_{channel} in this diffusive limit is[46]

$$R_{channel}(V_g) = \frac{h}{4e^2}\frac{L}{l_0} \approx 6.5\text{k}\Omega\frac{L}{l_0}, \tag{2.18}$$

where l_0 is the mean free path of charge carriers, L is the length of the CNT. To model the gate voltage dependent current through the channel we used the Landauer-Buttiker formula

$$I_{LB} = \frac{2e}{h}\int_{E_F+\frac{E_g}{2}}^{\infty}(f(E) - f(E - eV_{sd}))dE + \frac{2e}{h}\int_{-\infty}^{E_F-\frac{E_g}{2}}((1-f(E)) - (1-f(E-eV_{sd})))dE, \tag{2.19}$$

where $f(E)$ is the Fermi distribution and the first integral corresponds to electron transport and the second integral corresponds to hole transport.

$$f(E) = \frac{1}{1+\exp((E-E_F)k_BT)} \tag{2.20}$$

We can simplify Eqn. 2.19 by assuming that eV_{sd} is small and the difference in Fermi distributions can be approximated as $eV_{sd}\cdot df(E)/d(E)$. With this simplification we can rewrite Eqn 2.19, including current from both holes and electrons.

$$I_{electrons}(V_g) = \frac{2e^2}{h}\frac{l_0}{L}V_{sd}\left(\frac{1}{1+\exp\left((\frac{E_g}{2}-eV_g)/k_BT\right)}\right) \tag{2.21a}$$

$$I_{holes}(V_g) = \frac{2e^2}{h}\frac{l_0}{L}V_{sd}\left(1 - \frac{1}{1+\exp\left(\left(\frac{-E_g}{2} - eV_g\right)/k_BT\right)}\right) \qquad (2.21b)$$

The gate voltage V_g controls where the Fermi level sits in the band gap of the CNT. For example if $V_g > 0$, this will attract negative carriers into the CNT, effectively shifting the Fermi level up. In some cases the channel resistance dominates the total resistance of a CNT device. For example the channel resistance in a CNT is high when operated in the subthreshold regime. However, in most cases the contact resistance is also significant, so we consider the contact resistance next.

The second source of resistance in a CNT device is the contact resistance, which is controlled by the Schottky barrier and the wetting of the metal onto the CNT surface. Charge carriers from the metal cannot travel through the nanotube when they have an energy that is in the band gap. When there is a mismatch in work functions between the CNT and the metal, charges will redistribute themselves at the contact so that the bulk Fermi levels align. The position of the bands edges are pinned at the metal interface, but in the bulk of the CNT the band edges can be bent up or down by V_g. This can create a short distance tunneling barrier for charge carriers with energies within the valence and conduction band. This tunnel barrier is called the Schottky barrier, and an example of a Schottky barrier is shown in Fig. 2.3.

The potential where the bands are pinned at the metal is determined (to some extent) by the difference in work function between the metal and the nanotube, Φ_{metal} -

Φ_{CNT} (see figure 2.3). Interfacial states and trapped charge can also play a role. The potential at the metal-CNT interface for the valence band (Φ_V) and conduction band (Φ_C) is given by Eqn. 2.22.[48]

$$\Phi_C(x=0) = \frac{E_g}{2} - (\Phi_{CNT} - \Phi_{metal}) \tag{2.22a}$$

$$\Phi_V(x=0) = \frac{E_g}{2} + (\Phi_{CNT} - \Phi_{metal}) \tag{2.22b}$$

When there is no difference in work function the Fermi level of the metal will sit half way between Φ_V and Φ_C and the height of the Schottky barrier will be $E_g/2$. When there is a difference in work functions charges will redistribute themselves near the CNT–metal interface until the Fermi level of the metal and the Fermi level of the CNT are aligned. This redistribution of charges leads to built-in electric fields and band bending. Electrostatic doping will change where the Fermi level sits within the band, and the CNT will begin to conduct when the Fermi level approaches the valence or conduction band. There will be a Schottky Barrier to electrons when the bands are bent down, and a barrier for holes when they are bent up.

Palladium is a good choice of metal for making p-type transistors because its work function is 5.2 eV, which is about equal to $\Phi_{CNT} + E_g/2$. Palladium contacted CNT FETs have no barrier for hole injection for CNT band gaps up to 1 eV. Palladium also has good adhesion to CNTs.[49] Gold is also a good choice with a work function of 5.1 eV, and will have no hole barrier for CNT band gaps up to 0.8 eV. Gold also has fair binding to CNTs.[49]

The work function of gold and other metals are highly susceptible to change upon the absorption of molecules on its surface.[48] A CNT FET on SiO_2 with gold contacts makes a good p-type conductor in air because of the electrostatic doping from absorbed oxygen and the silicon oxide surface will bring the Fermi level closer to the valence band. Ideally a CNT FET is tailored so that the work function of the metal is compatible with the band gap of the CNT used in the circuit. Below is a diagram of how the bands bend when a CNT with E_g = 0.6 eV and is contacted by gold.

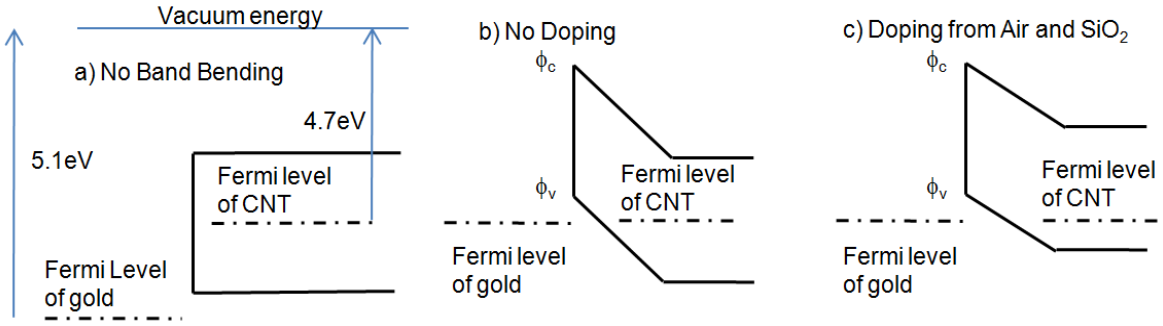

Fig. 2.3 CNT-gold junction. The diagram features a 0.6 eV bandgap nanotube with gold contacts. The work function of gold is 5.1 eV. Therefore, 5.1 eV of energy is required to move an electron from gold to vacuum. The work function of the CNT is 4.7 eV. b) Electrons at the CNT gold contact will move to balance out the discontinuity in potential and the fermi level of the nanotube bends down to the fermi level of the gold. This creates an ambi-polar device, with a tunnel barrier to n-type conductors. c) A CNT FET in air on a silicon oxide surface will experience electrostatic doping from oxygen and charges in the silicon oxide. These negative dopants will shift the fermi level down and will make a p-type device.

We modeled the effects of the Schottky barrier for a liquid-gated CNT FET. The metal has a fixed potential, but the local potential of the CNT can vary. The gate voltage will change the potential of the CNT, or in other words the gate voltage changes the Fermi level relative to the band edges. Since band bending is caused by Fermi level realignment, the gate voltage also controls band bending. We estimate the length to adjust

potentials for band bending as the thickness of the Helmholtz layer in solution (0.2 to 0.7 nm). Therefore the maximum length charge carrier will have to tunnel is set to about 3 angstroms. The probability of tunneling through the barrier can be found using the WKB approximation. We modeled the barrier as a triangle of height defined by Eqn. 2.22 and the applied gate voltage. For example refer to Fig. 2.3b, electrons at energies above the conduction band but below Φ_C will have to tunnel through a Schottky barrier.

$$P(V_g, E) \approx \exp(-4\pi \int_o^{x_b} \sqrt{\frac{m(V(x, V_g) - E)}{h^2}})dx \qquad (2.\ 23)$$

Where m is the effective mass of the current carrier, $V(x, V_g)$ is the height of the potential barrier, and E is the energy of the current carrier. For example we can calculate the probability of tunneling through the barrier shown in Fig. 2.3b for an electron with an energy of half the barrier height to be 83%.

We can include this tunneling probability into the Landauer-Buttiker formula shown in Eqn. 2.19 and find an expression for the current through the valence and conduction bands.[37]

$$I_C = \frac{2e}{h}\frac{l_0}{L} \int_{E_F + \frac{E_g}{2}}^{\infty} P(V_g, E)(f(E) - f(E - eV_{sd}))dE \qquad (2.\ 24a)$$

$$I_V = \frac{2e}{h}\frac{l_0}{L} \int_{-\infty}^{E_F - \frac{E_g}{2}} P(V_g, E)((1 - f(E)) - (1 - f(E - eV_{sd})))dE \qquad (2.\ 24b)$$

Figure 2.4 is a plot of the conductance of a nanotube as a function of gate voltage, found using equation 2.24. There are 2 free parameters used to create this fit, E_g, l_0, and all other parameters are estimates defined by the conditions of the experiment.

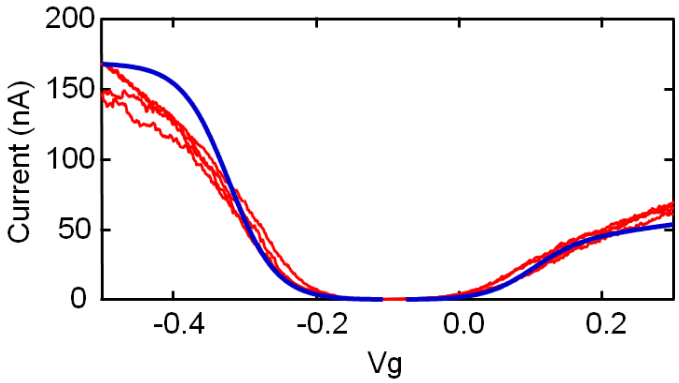

Fig 2.4 Conduction model applied to a CNT FET circuit. The red curve is a CNT transistor curve taken from a circuit made in our lab with gold contacts. The blue curve is model data created with equations 2.24. The model uses the known values of the work functions Φ_{metal} = 5.1 eV, and Φ_{CNT} = 4.7 eV, and an electron mass of 9.1×10^{-31} kg. It also uses the theoretical values for a tunneling barrier length of 0.3 nm, and the nanotube gate voltage coupling constant of 0.8. We needed to fit 2 parameters E_g = 0.34 eV, and l_0=350 nm, and both parameters fall within a reasonable range.

With this relatively simple model we are able to explain the $I(V_g)$ behavior of the CNT FETs produced in the lab. This model is powerful because it shows how to tune the fabrication to produce the best device. For example, we now know how to choose the metal to fit the nanotube band gap of the CNT, and choose CNTs with an appropriate E_g.

2.3.1 Capacitance of CNTs in solution

The voltage applied by the reference electrode is not the same as the voltage experienced by the CNT. This is because there are multiple capacitive elements in series between the CNT and the reference electrode. The first capacitive term is from the double layer and is given by Eqn 2.17. To find the double layer capacitance around the nanotube

we estimate the effective area as being half of a 2 nm diameter cylinder. The double layer capacitance per unit length is then calculated from Eqn. 2.17

$$C_{dl} = \frac{\pi(diameter)}{2} C_{dl} \approx 2x10^{-9} F/m \tag{2.25}$$

The second capacitive term is the quantum capacitance. As the Fermi level of the CNT changes, electrons will fill in the unoccupied states. The quantum capacitance is the number of electrons per volt shift in the Fermi level (Q/V). We can find the quantum capacitance by finding the density of states $D(E)$. The spacing between wave states Δk is

$$\Delta k = \frac{2\pi}{L} \tag{2.26}$$

Where L is the length of the CNT. The energy spacing ΔE is therefore

$$\Delta E = \frac{\hbar v_F \Delta k}{4} = \frac{h v_F}{4L} \tag{2.27}$$

Here there is a factor of 4 to account for the 4 fold degeneracy of charge carriers in a CNT. The density of states $D(E)$ is the inverse of the energy spacing. To convert this to capacitance we multiply by a factor of e to go from volts to energy and another factor of e to go from number of electrons to coulombs.

$$C_q = e^2 D(E) = \frac{e^2}{\Delta E} = \frac{4Le^2}{h v_F} \approx 2x10^{-10} F/m \tag{2.28}$$

The constant value approximation is accurate except near the transistor off state. To find the total capacitance C_T we combine the capacitance in series

$$\frac{1}{C_T} = \frac{1}{C_q} + \frac{1}{C_{dl}} \tag{2.29}$$

With an estimate for both capacitance terms in series we can find the relationship between the change in Fermi level in the CNT and the applied voltage. The charge *Q* is determined by $C_T V_g$. With capacitors in series, the charge *Q* on each capacitor is the same. The voltage drop across the quantum capacitor V_q, is the voltage that controls the shifting of the Fermi level and is given by

$$V_q = \frac{Q}{C_q} = \frac{C_T V_g}{C_q} \approx 0.8 V_g \tag{2.30}$$

2.3.2 Temperature dependence

Temperature fluctuations can be a source of systematic error for nanoFET biosensor experiments. Changes in temperature can be introduced when warmer or cooler liquids are introduced to the microfluidic system. The most sensitive operating point for biomarker detection is when the Fermi level is within the band gap (subthreshold region).[8] This operating point is also sensitive to temperature changes. We can simplify Eqn. 2.21 for the specific case of operation in the subthreshold region (Threshold voltage $eV_{th} = E_g/2$). The conductivity depends exponentially on temperature [50]

$$G = G_o \exp\left(\frac{-e(V_g - V_{th})}{k_B T}\right) \tag{2.31}$$

Figure 2.5 illustrates how temperature sensitivity depends on V_g. At a typically operating point ($V_g - V_{th}$ = 200 mV) conductance can swing by over 2% for a temperature change of 1°C. The issue of temperature control can be addressed by actively correcting

temperature fluctuations using an on-chip temperature sensor and heater. An alternative, low-tech approach is to let all solutions equilibrate to room temperature before beginning a measurement.

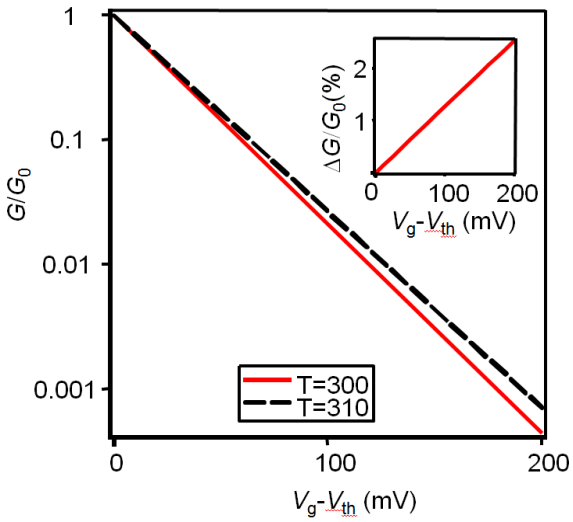

Fig. 2.5 Temperature dependence of a CNT FET. The plot shows the conductance as a function of the difference between gate voltage V_g and the threshold voltage V_{th}. The insert shows the percent change in conductance for a temperature difference of 1°C.

2.4 Carbon Nanotubes Transistors as Biosensors

The goal of this work is to create label-free biological molecule sensors using CNT FETs. To make a biosensor the CNT FET must be integrated with biological conditions. This section discusses the various mechanisms by which a FET sensor can respond to absorbed protein.

There are four ways a CNT FET sensor can respond to absorbed protein, each with a characteristic signal.[37] The four types of responses are illustrated in Fig. 2.6. Carbon nanotube electrostatic doping (Fig. 2.6a) happens when charged proteins come near the CNT and change the local potential. This is equivalent to a shift in the applied

gate voltage. Electrostatic doping should be distinguished from chemical doping, where the bulk atoms are replaced with a dopant to increase conductivity.

When proteins bind to the metal contacts they can change the effective work function of the metal (Fig. 2.6b). This changes the barrier height as shown in Eqn. 2.22 and generates an asymmetric response.

Proteins that land on the CNT surface can coat the surface and create a barrier between the CNT and the charged ions in solution (Fig. 2.6c). This effectively creates a capacitor in series with the capacitance found in Eqn. 2.29. We can make an estimate for the capacitance of the protein film assuming 1 nm thick film, with an area of a 2 nm diameter half cylinder, and a relative permittivity of 30, which gives a capacitance of $8x10^{-10}$ F/m. This additional capacitance reduces the capacitive coupling constant and a greater applied voltage is needed to generate the same transistor response.

Lastly, bound protein may change the scattering length l_0 of the carriers in the carbon nanotube effectively changing the resistance in the channel (Fig. 2.6d).

Typical biosensing data shown in chapters 4 and 5 can usually be explained by the doping mechanism. Sensing experiments on IgG (chapter 5), which is a large, neutral molecule, still show that doping is the dominant effect.

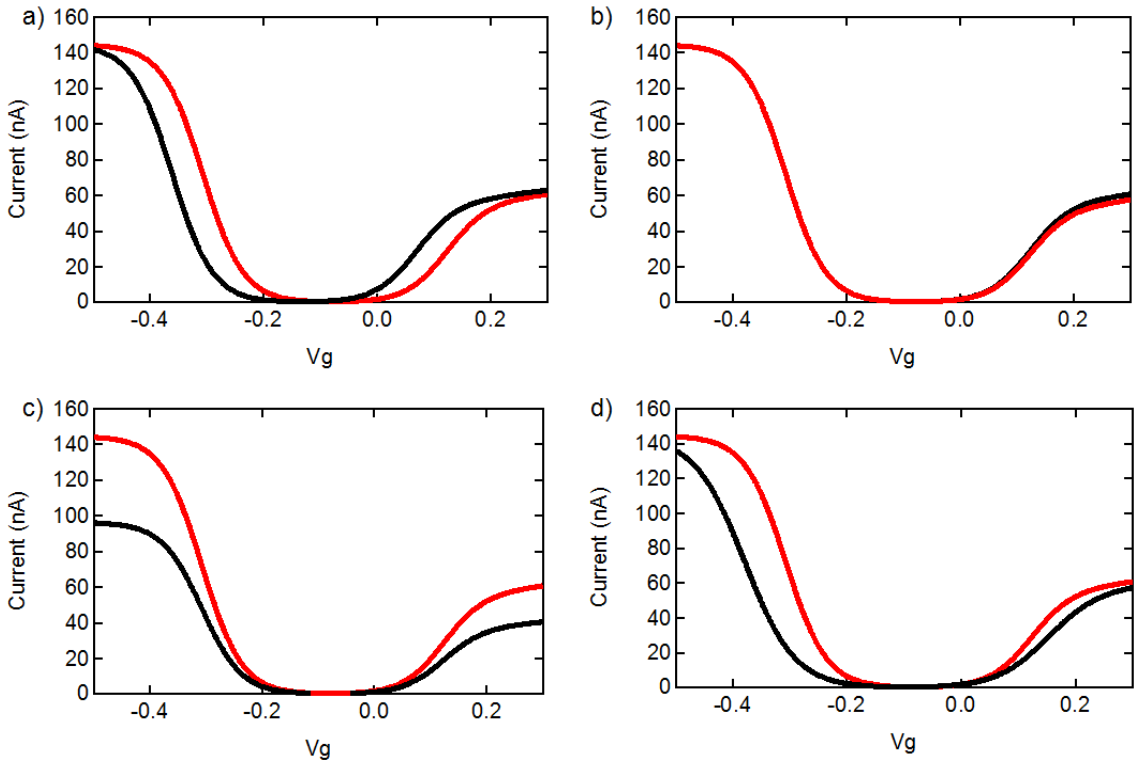

Fig. 2.6 Effect of absorbed protein on CNT FETs. This figure illustrates the different ways a CNT FET sensor can respond to absorbed protein. The curves are generated using Eqn. 2.24. a) 40 mV electrostatic doping shift gives a characteristic linear translation b) A 40 mV increase in the metal work function produces an asymmetric effect on the curve by increasing the tunneling probability for electrons to the conduction band c) Reduction in the capacitive coupling by introducing a 1 nm thin film of protein with a relative dielectric constant of 30. This reduces the gate coupling from 88% to 67% d) Reduction in the effective scattering length from 300 nm to 200nm

2.5 Conclusion

We are able to predict the behavior of a CNT FET transistor with a conductance model based on the Landauer formula and the Schottky barrier. Using the Stern model we are able to predict the electrostatic potential at the surface of a CNT FET device. By analyzing the effect of temperature on CNT we are able to identify a potential source of systematic error in biosensor experiments.

CHAPTER 3

EXPERIMENTAL SET-UP

This chapter discusses details of CNT transistor fabrication, measurement, and biosensor implementation. Carbon nanotubes are grown by chemical vapor deposition (CVD) and then transistors are patterned using photolithography and other micro-fabrication techniques. The CNT circuits are imaged and then probed electrically in a low noise environment. Finally the CNT transistors are integrated into a solution environment for bio-sensing applications using microfluidics.

3.1 Circuit Fabrication

Many fabrication processes have been developed for nanotube transistors. [51,52,53] The transistor devices made in this work can be broadly classified as (i) devices with only a few CNTs per circuit and (ii) network devices with many CNTs per circuit. We have tried both types of devices and the pros and cons of each type are described below.

The first type of CNT circuit was fabricated by patterning nanotube catalyst onto the device substrate and then growing CNTs directly onto a silicon wafer using catalyzed chemical vapor deposition (CVD).[51] The number of CNTs completing the circuit follows random Poissonian statistics. Our fabrication process has been tuned so that there will likely be one or more CNTs forming a complete circuit, although not all devices will form a complete circuit.

The second style of circuit is the network device. Network devices typically involve fewer fabrication steps and higher yields of working circuits. [52,53] However, these

network devices do not give us insight into transduction mechanisms at the single CNT level. Sensors with only one CNT are more promising than network sensors for single molecule sensing applications.

3.1.1 Carbon Nanotube Growth Using Chemical Vapor Deposition

Catalyzed CVD growth of nanotubes is performed in a one-inch tube furnace using growth parameters based on an existing recipe.[54] Wafers are patterned with CNT catalyst and are diced into 2x2 cm sections (small enough to fit in the one-inch tube furnace). The 2x2 cm chip is then annealed in open air at 750 °C for 5 min. The furnace is then sealed, flushed with argon, and annealed with H_2 at 0.45 SLM for 10 min to remove oxygen from the metal catalyst. The furnace is flushed again with argon and ramped up to the nanotube growth stage at 900 °C. The gases during growth are 0.45 SLM H_2, 0.15 SLM Ar bubbled through ethanol, and 0.3 SLM Ar bubbled through methanol. The growth time is 15 min. The furnace is then cooled under an Ar flow. This growth technique produces CNTs with a range of diameters, from 1-3 nm. A schematic of the CVD furnace is shown in Fig. 3.1

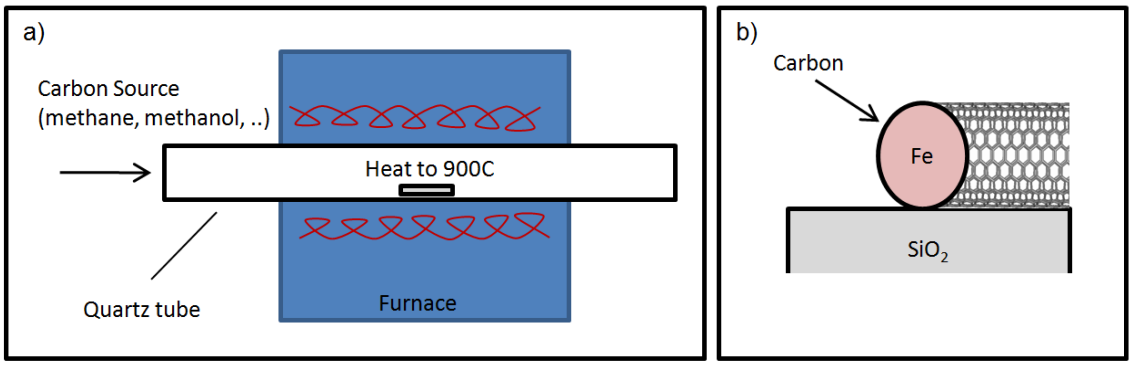

Fig. 3.1 Carbon nanotube growth by CVD. a) A carbon based gas is flowed through a quartz tube furnace, where the gas interacts with a silicon chip covered in CNT catalyst. b) Iron based CNT catalyst on a silicon wafer during the CVD process. Carbon dissolves into the iron catalyst and excess carbon is excreted as a carbon nanotube

CNT growth done at lower temperatures favors shorter nanotubes with smaller diameter, and smaller yields,[29,55] (Almaqwshi et al. to appear in Nanotechnology). Smaller diameter semiconducting CNTs have larger band gaps (Eqn. 2.1). Large band gap CNTs may be more desirable for FET sensors, and therefore the CNT growth temperature can be a compromise between yield and band gap. The diameter of a CNT can be checked relatively easily with an atomic force microscope after growth.

There is a large variety of catalysts that will grow CNTs using CVD. One method we have tried uses alumina supported CNT catalyst dissolved in DI water, which is deposited onto the surface by drop-casting.[51] This catalyst solution has 1.3 mg/ml iron nitrate $Fe(NO_3)_3$, 0.3 mg/ml Molybdenum (VI) dioxide bis(acetyl-acetonate), and 1 mg/ml of nano-powdered alumina (Al_2O_3 from Degussa). A second method is our spun-on catalyst, which is a solution of 1 mg/ml PVP (polyvinylpyrrrolidone MW 360 kDa) (Sigma Aldrich), 1 mM iron nitrate (Sigma-Aldrich), and 0.5 mM Molybdenum (VI)

dioxide bis(acetyl-acetonate) (Strem Chemicals).[54] The PVP increases the viscosity of the solution to give a uniform spin coat. Lastly, electron beam evaporation can be used to deposit a catalyst film of pure iron with a target thickness of 0.2 nm.[52]

Horizontal CNT growth on surfaces can be classified into two categories, aligned growth and random orientation growth. In our aligned growth, nanotubes grow in a straight line because they are grown on a quartz wafer and the CNTs follow the crystal axis as they grow.[52] Our random growth is usually done on silicon oxide and the CNTs have no preferred growth direction. Examples of random and aligned growth are shown in Fig. 3.2

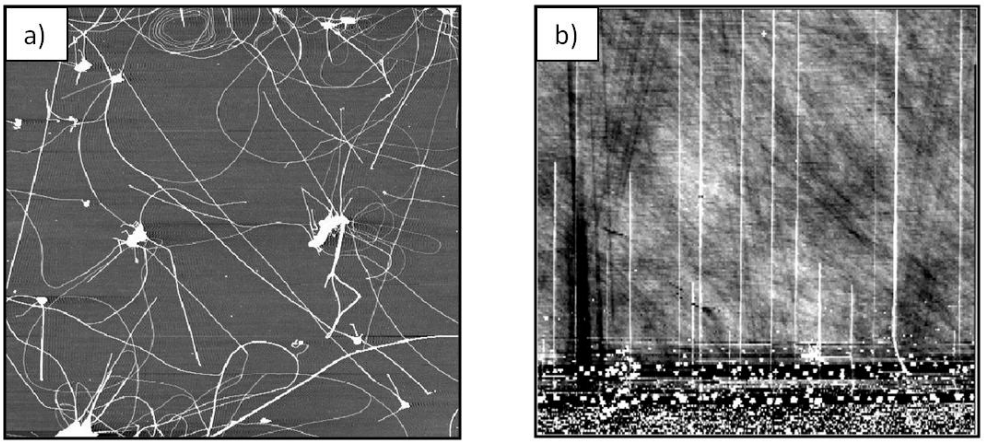

Fig. 3.2 AFM images (10x10 μm) of CNTs grown by CVD. a) Un-aligned CNTs grown with alumina supported catalyst on SiO_2 b) Horizontally aligned CNTs on ST-cut quartz grown with evaporated iron

The PVP catalyst can be used to coat whole chips with CNT catalyst. These chips can then be grown to produce dense networks of tubes. This can be done on quartz for aligned tubes or as a random network on silicon oxide.

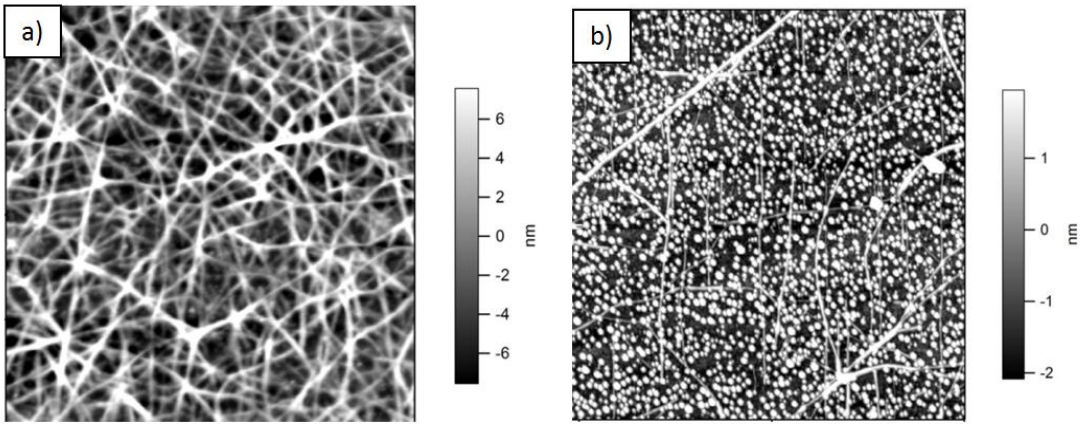

Fig. 3.3 AFM images (2x2 μm) of CNTs grown by spin coating PVP catalyst a) Network of CNTs grown on a silicon oxide surface b) CNTs grown on ST-cut quartz showing partial alignment of the CNTs. Alignment is likely inhibited by the high density of catalyst.

These dense networks of nanotubes can then be patterned using photolithography and an oxygen plasma cleaner. Patterned photoresist covers areas of desirable CNTs and leaves unwanted CNTs exposed to oxygen plasma, which are then removed.

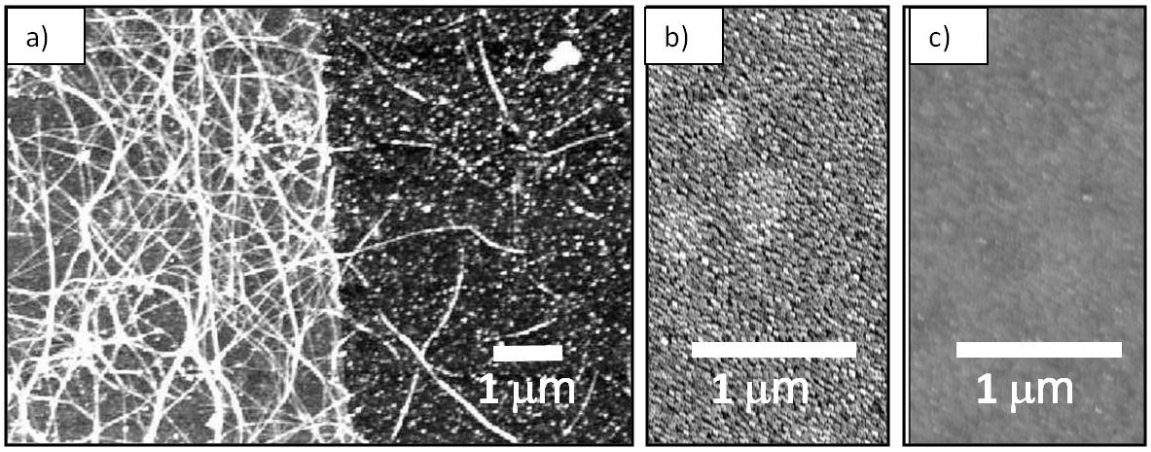

Figure 3.4 AFM images of patterned CNT networks a) Network of CNTs grown with a PVP catalyst. After growth the network was patterned with photolithography and the exposed areas are oxygen plasma cleaned for 10min to remove unwanted CNTs b) The cleaned surface after 25min of O2 plasma c) cleaned surface with an additional 15sec etch in 20:1 buffered HF to remove inorganic residue.

Most of our biosensing work was done using a few CNTs per circuit grown at 900°C, with random orientation. Aligned CNTs on quartz are desirable for predictable circuit fabrication. However, using quartz results in the loss of a conducting backgate. To regain a backgate CNTs must be transferred onto a SiO_2/Si wafer.[56,57] Randomly oriented CNTs are simpler to fabricate and serve the same biosensor function as aligned CNTs. Most of the devices used in the course of this thesis are randomly aligned and are grown at 900 °C because we observed the greatest return on complete circuits at this temperature.

3.1.2 Fabrication of CNT FETs with a few CNTs

The CNT transistors used in chapters 4 and 5 are created on silicon wafers that are p-doped and have a 300 nm top-surface oxide (Silicon Quest, Nova Electronics). An example of a finished device is shown in Fig. 3.5.

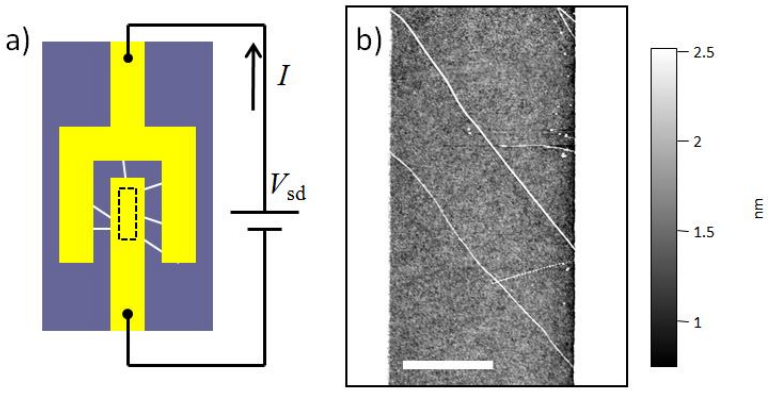

Fig. 3.5 Carbon nanotube field effect transistor circuit. a) Source and drain electrodes (yellow) are connected by 5-10 CNTs (white lines). The dashed line indicates the 6x46 μm rectangle where catalyst is deposited. V_{sd} is held constant at 25 mV and I is monitored by a current pre-amplifier (not shown). b) AFM image of two CNTs connecting source and drain electrodes. Scale bar 2 microns.

Before CNT growth, alignment markers are patterned onto the chip using photolithography as shown in Figure 3.6 a-c. The photoresist (S1813 from Microchem) is spun to a nominal thickness of 1.3 μm and patterned using a contact aligner (Karl Suss). After development, the photoresist is hard-baked (5 min at 115°C) to prepare the resist for an oxide etch. Alignment markers are etched into the SiO_2 using buffered HF (20:1 buffer to HF ratio, total etch depth 100 nm).

To selectively deposit catalyst on the chip (Figure 3.6d-e), a second photolithography step is performed. A wafer with patterned photoresist (S1813) is exposed to catalyst by either drop casting a catalyst solution,[51] spinning on a catalyst solution,[54] or electron-beam evaporation of a thin metal layer.[52] All three catalysts produce good results. Once the catalyst has been deposited, the photoresist is removed by rinsing sequentially with acetone, isopropyl alcohol, and DI water. Small rectangles of catalyst are left behind.

The last step of circuit fabrication is the deposition of metal electrodes (Figure 3.6 g-i). The chip is coated with a bi-layer photoresist (LOR3B and S1813 from Microchem). The under-layer (LOR3B) ensures an undercut profile which aids in metal lift off (Fig. 3.6j). After patterning the photoresist, the chip is placed in a thermal evaporator. The electrodes metals are Cr/Au (1-5 nm/30 nm). The Cr layer promotes adhesion of the Au to the oxide surface. A 1 nm Cr adhesion layer yields better electrical contact to the CNTs than thicker Cr layers. The evaporation rate is 0.1 nm/s and residual gas pressure is $7x10^{-6}$ Torr or lower. After the metal deposition, photoresist and excess metal is lifted off

by soaking in remover (Remover PG from Microchem) at 60 to 80°C for 1 hour. The chip is rinsed sequentially with acetone, isopropyl alcohol, and DI water before drying.

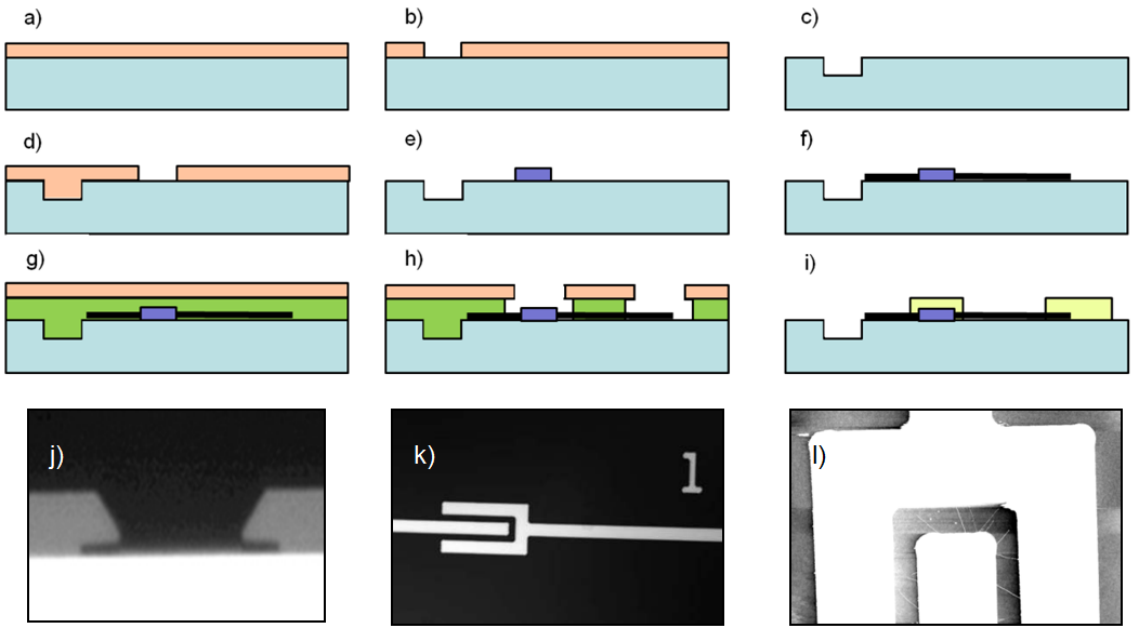

Fig. 3.6 The biosensor device fabrication process. a) Photoresist is spun onto a silicon wafer. b) Photoresist is soft-baked, exposed, developed, and hard-baked. c) The oxide is etched and the photoresist is removed. d) The wafer is patterned with photoresist again, preparing for catalyst deposition. e) Catalyst is deposited onto the wafer and the photoresist is removed. f) Nanotubes are grown by CVD. g) Bi-layer photoresist is spun onto the wafer. h) The photoresist is patterned and ready for metal evaporation. i) Cr/Au is thermally evaporated onto the wafer, and the photoresist is removed. j) Optical microscope image of a cross section of bi-layer photoresist showing an undercut. k) Optical microscope image of a completed circuit. l) AFM image of a complete circuit with CNTs.

The process described above is tuned so that most circuits have a total of 5-10 CNTs and 1 or 2 CNTs making good contact to the electrodes. We can check the conductivity of an individual CNT using Electrostatic Force Microscopy (EFM) and see which tubes are well connected to the metal (see Fig. 3.7).[58]

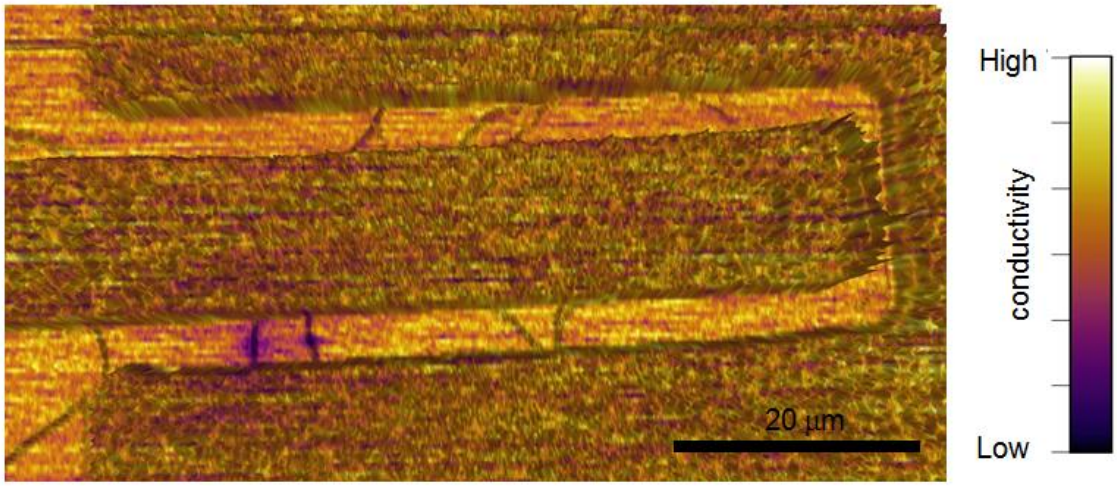

Fig. 3.7 Scanning gate microscopy image on a CNT FET. This is a scanning gate image superimposed onto a EFM phase image. We can see that 10 tubes appear to be connected but only 2 of the 10 show a gate response when a highly charged AFM passes over. This indicates that only 2 CNTs are well connected. Image courtesy of Landon Prisbrey.

We chose to fabricate our circuits in this way because of a balance of ease of fabrication, yield of working circuits, and cleanliness. Attempts to make network CNT circuits (Fig. 3.4) were hampered by surface functionalization issues, see below.

3.1.3 Fabrication of Network CNT Circuits

Network CNT circuits are made in a similar way as the previous style of circuits but requires fewer alignment steps. The PVP catalyst is spun onto the whole chip surface and then CNTs are grown using the same CVD process. This leaves a dense network of nanotubes on the whole surface, as shown in Fig. 3.3. Metal electrodes are patterned onto the chip with the network of nanotubes as described in the same way as described in section 3.1.2. Advantages of the network technique are that it does not involve an

alignment step for patterning the catalyst or electrodes, close to all of the circuits are functioning FETs, and the FETs have comparable properties.

An example of a biosensor experiment done using a network sensor is shown in Fig. 3.8. The ratio of fluctuations in current to absolute current is approximately 1 nA/ 900 nA. This is a better ratio that we typically observe in devices that are made with a few CNTs. Noise caused by random fluctuations in CNT resistance grows like the square root of the number of CNTs, while the signal will increase linearly with the number of CNTs.

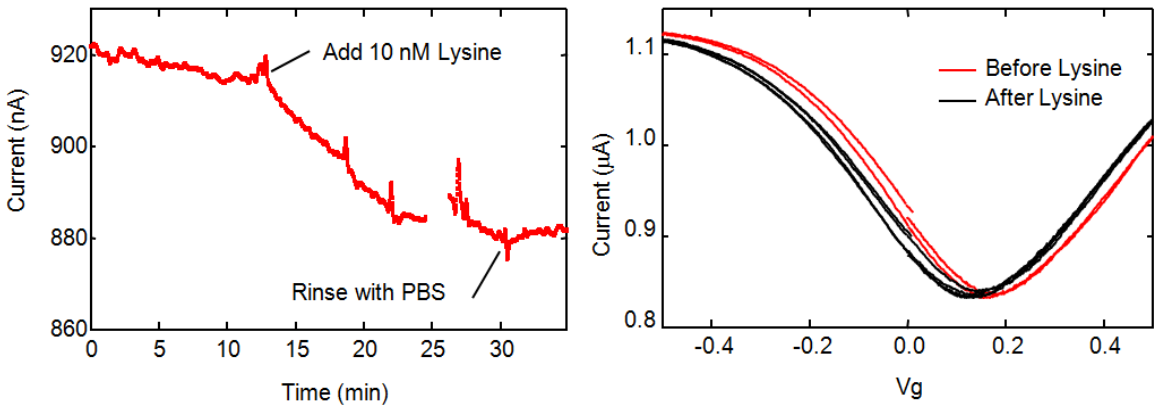

Fig 3.8 Poly-L-lysine sensing experiment on a network CNT sensor. At around 10 min PLL is added and the sensor changes conductance then eventually saturates after about 11 more minutes. The high frequency noise of this circuit is low compared to a simlar circuit made with only a few CNTs. However, there are occasionally large spikes in conductance.

We did encounter some prohibitive problems with the network style sensors. The most important was that the fluorescence images did not show our model protein poly-L-lysine on the surface of the CNT network (see chapter 4). This could be due to either

fluorescent quenching of the FITC tag by the CNT[59], or simply the poly–L-lysine was not sticking to the CNTs. This is shown in Fig. 3.9.

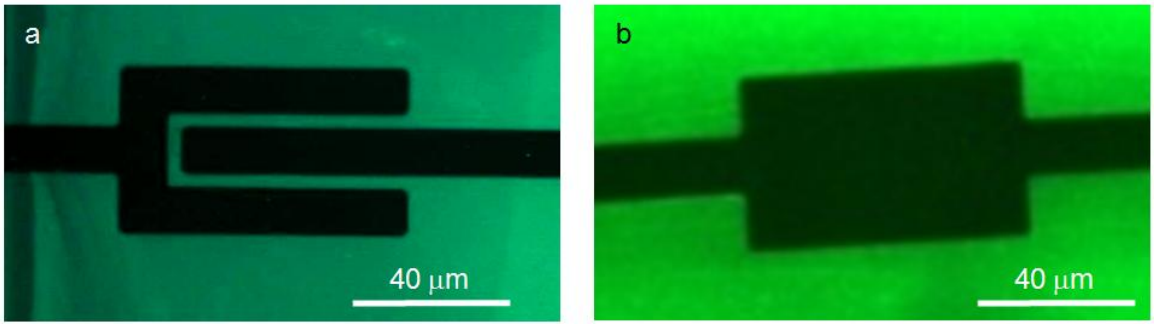

Fig. 3.9 Fluorescence of FITC tagged polylysine on CNT networks. a) Fluorescent polylysine on a SiO_2 based CNT sensor. Fluorescence is visible everywhere except the gold electrodes. The CNTs of the FET do not interfere with fluorescence b) This fluorescence image illustrates the lack of fluorescence on a dense network of CNTs patterned with O_2 plasma (refer to Fig. 3.4). There are no gold electrodes in this image, only CNTs. For details on PLL experiments refer to chapter 4.

We observed larger low frequency noise in the network circuits. This can be seen in the spikes of Fig 3.8. This is perhaps caused by a few CNTs that are poorly connected and are switching between being connected and not connected. This type of noise is problematic for biosensing since the signals from proteins occur at the same time scales.

Despite the easy fabrication process and high yield of consistent FET transistors we decided not to pursue network style circuits. Our networks of CNTs did not show fluorescence of tagged protein on the CNT surface. Fluorescence measurements are important for protein flux quantification (see chapter 4), and we decided this quantification was more important than easy fabrication.

3.1.4 Cleaning chips

Having clean CNT chips is important for consistency in bio-sensing experiments. Previous authors have noted the importance of this step before selective functionalization of CNTs can be achieved (see chapter 5),[60] and a clean reproducible surface is important for consistent protein adsorption. The photoresist used during fabrication leaves organic residue on the circuit. An effective way to clean the circuit before a biosensing experiment is to anneal for 10 minutes at 400°C in an Ar atmosphere (1 SLM Ar in a one-inch tube furnace).[61] The effect of annealing is shown in Fig. 3.10. The annealing step affects the device properties, often increasing the contact resistance between the metal and the CNT. This may be due to oxidation of the Cr sticking layer.

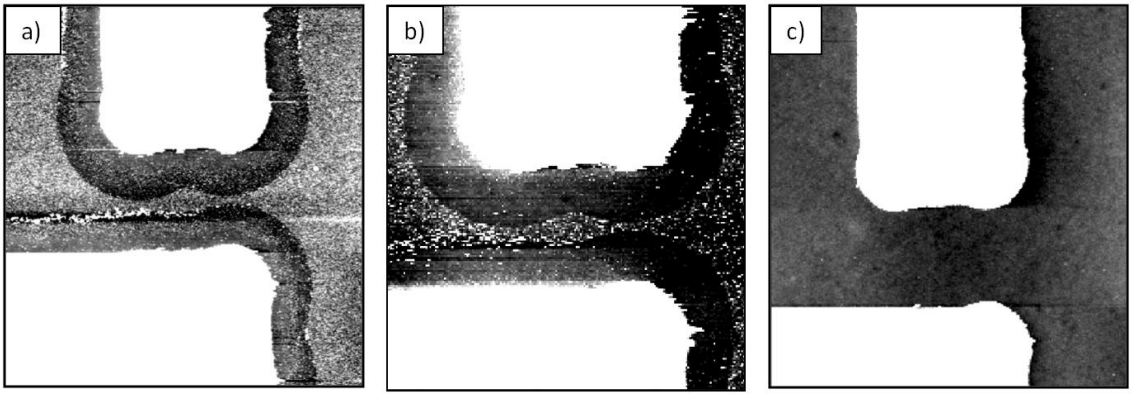

Fig. 3.10 AFM images of surface cleaning. a) Metal electrodes (white) and the oxide surface directly after lift-off in room temperature remover. The electrodes are 10 μm wide. The undercut causes the outline around the electrodes, refer to Fig. 3.6j B) The same circuit after a 2 min cleaning in fuming nitric acid c) The same area after a 10 minute anneal in 1 SLM Ar at 400°C. The height scales for all images are identical. There are no CNTs in this test circuit.

We also tried using buffered hydrofluoric acid to clean CNT chips after fabrication. The HF successfully removed the top layer of silicon oxide (8 nm by AFM) but seemed to causes hydrophobic residue to be deposited onto the CNT surface.

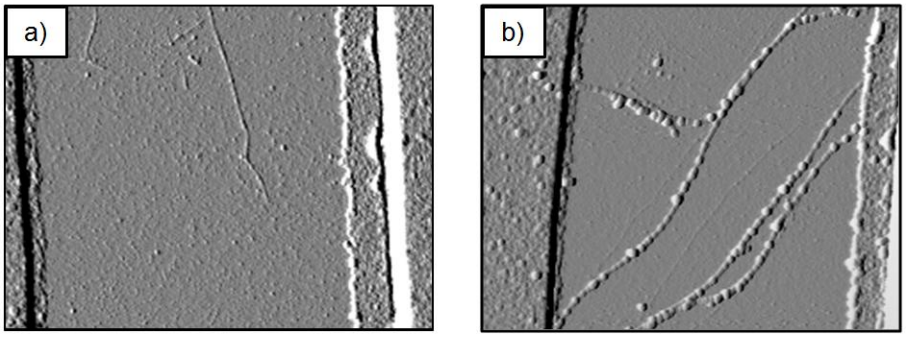

Fig. 3.11 Hydrofluoric acid cleaning of CNT FETs. The images are AFM amplitude scans of a CNT FET, where the spacing between metal electrodes is 4 μm. a) A CNT chip after lift-off of photoresist b) The same chip after an attempt at cleaning the surface by removing 8 nm of silicon oxide with HF. It appears that the HF treatment causes hydrophobic material not soluble in HF to bind to the nanotubes. The treatment may clean the oxide surface but is not useful for cleaning CNT circuits.

Most of the CNTs circuits used in our experiments are cleaned with PG remover at 80°C before a bio-sensing experiment and produce clean circuits as shown in Fig 3.11a. We found that this was sufficiently clean and consistent to give repeatable results. The furnace annealing usually does give cleaner surfaces but almost always results in an increase in FET noise. We observed that the surface cleanliness after the remover allowed for significant protein binding and we decided it was more important to have lower noise circuits.

We pursued using the enzyme trypsin to clean our sensors. After performing a PLL sensing experiment we would like to clean the SiO_2 surface and repeat the experiment. Trypsin is an enzyme that will cleave peptide chains at the amino acids

lysine and argenine. Trypsin is known to dissociate cells from a surface and can be purchased at Sigma Aldrich. In the experiment shown below, a CNT FET is treated with a concentration of 10 μg/ml poly lysine. The sensor is then rinsed with buffer to remove loosely bound poly lysine. The sensor is then treated with 5 mg/ml solution of trypsin and allowed to react for about 30 min. After the addition of trypsin the sensor is rinsed again with buffer and the sensor shifts by 40 mV beyond the previous buffer rinse. This suggests that trypsin has broken up and removed absorbed poly lysine more effectively than rinsing with PBS. This experiment is shown in Fig. 3.12. Unfortunately the trypsin only removed a fraction of the absorbed poly lysine and does not create a sensor that is clean enough for reuse. For future researchers we suggest alternating layers of positively charged PLL and negatively charge SS-DNA.[62] Alternating layers may be an effective way to perform multiple experiments on the same device.

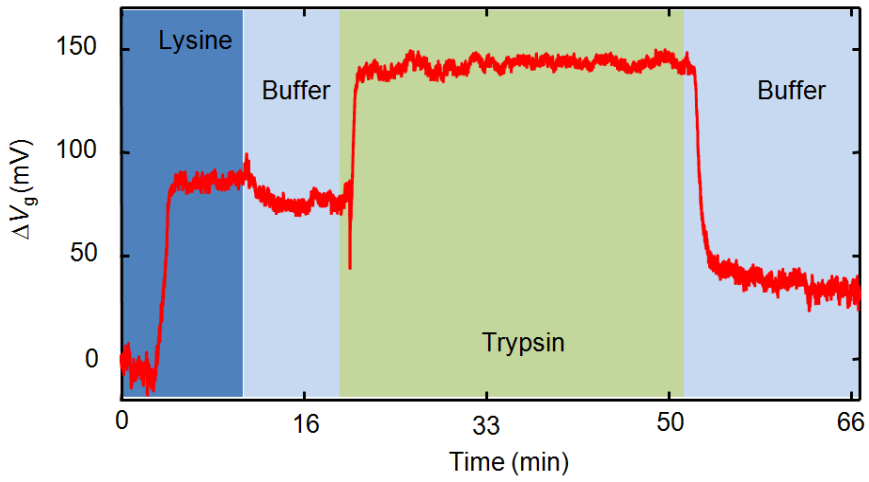

Fig. 3.12 Removing polylysine with trypsin. First there is addition of 10ug/ml poly lysine, then a buffer rinse that changes the surface potential by 10 mV. Trypsin is then added and rinsed off with buffer. The potential after the buffer rinse is 40 mV less than the rinse after lysine suggesting that trypsin removed 40 mV worth of poly lysine bound to the sensor surface.

3.2 Probe Station and Measuring CNT Circuits

All electrical measurements of CNT circuits were taken inside a Farday cage using micromanipulator needles that contact the gold electrodes of the CNT circuit. The source-drain voltage V_{sd} and gate voltage V_g are supplied by a National instruments DAQ board (NI USB 6251). The DAQ voltage is fed through a 100:1 voltage divider to lower the noise from the DAQ. Usually we set V_{sd} = 25 mV. This voltage corresponds to thermal energy k_BT, and was chosen because it is very unlikely to damage a nanotube, but is high enough to easily measure current. The current is measured with a current preamplifier (Stanford Research Systems SR570), which then outputs a voltage signal to the DAQ analog to digital converter. The current amplifier has a tunable low pass filter, which we usually set to 1 or 10 Hz. Most bio-sensing experiments respond with time

scales on the order of minutes, so high frequency noise can be filtered out. A diagram of the probe station set-up can be found in Fig. 3.13

Having a well connected instrument ground is important for probe station measurements. All probe needles use coaxial cables up to the micromanipulator, and all have their shielding grounded to a common point (star grounding). All other grounds are connected to this common point. For example the Faraday cage, syringe pump shielding, DAQ board ground, and current amplifier ground, are all connected to the common point. A circuit diagram is shown in Fig. 3.13c.Using this configuration ensured that the probe station noise level was less than the noise generated by the CNT FET.

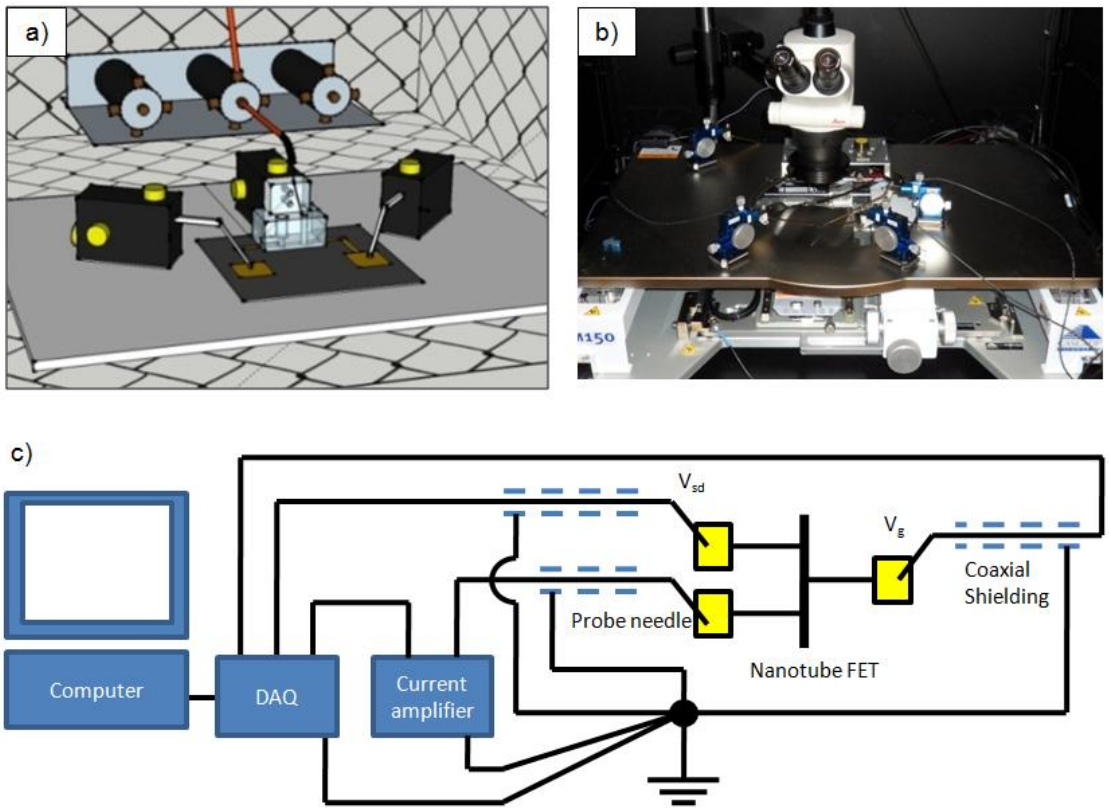

Fig. 3.13 Probe Station a) Cartoon of probe station showing probe needles and microfluidic setup connected to a CNT chip. The whole experiment is surrounded in a Faraday cage to reduce noise. The image is not drawn to scale. b) photo of the probe station, Fig. 3.14 shows a close up of the chip and microfluidics. c) Circuit diagram of the probe station.

3.3 Microfluidics

3.3.1 Fluid delivery to the biosensor chip

Microfluidic channels made from polydimethylsiloxane (PDMS) are a well established method to deliver small volumes of solution to the active area of a biosensor.[63] PDMS channels can form temporary or permanent seals to silicon wafers and have potential for "lab on a chip" applications. We have chosen a simple rectangular

channel geometry because it is easy to make and the geometry is easy to model in finite element modeling software. A diagram of the PDMS channel is shown in Fig. 3.14. With a known fluid velocity profile the theoretical flux of protein can be calculated (see chapter 4). This theoretical protein flux is useful to compare to experiments.

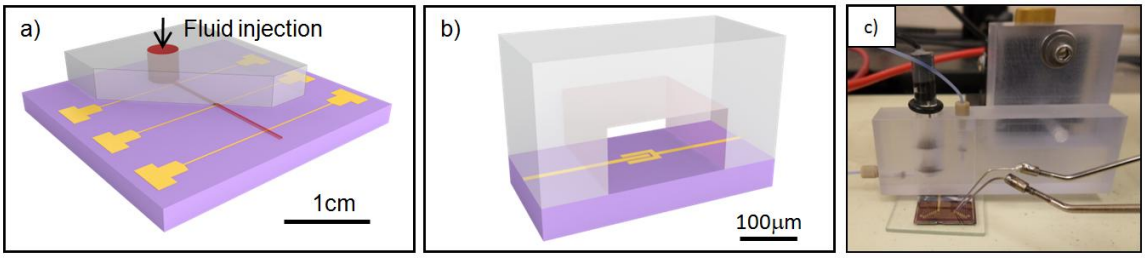

Fig. 3.14 Microfluidic setup a) Cross section of a PDMS channel (gray) on our CNT FET biosensor chip (purple). Fluid is colored red for clarity. b) Magnified image showing the gap between electrodes and the width of the microfluidic channel. c) Photo of acrylic PDMS clamp on a CNT chip with probe needles

The mold for creating a PDMS flow channel is made from 100 µm thick photoresist (SU8 3050 from Microchem). The photoresist mold is patterned in a contact aligner and then developed following the manufacturer's guidelines. PDMS is mixed (10:1 ratio of resin to hardener) and then poured on top of the photoresist mold. The PDMS is cured overnight at room temperature and then removed from the mold. The resulting flow channels are 100 µm tall and 200 µm wide.

The PDMS channel is pressed onto a CNT FET biosensor chip to form a water-tight seal with the oxide surface. We use a home-built acrylic fixture to clamp the PDMS in place (Fig. 3.14c). The fixture connects to inlet and outlet tubing (Teflon tubing, 0.009in inner diameter, Upchurch Scientific) and holds a Ag/AgCl reference electrode (model MF-2078, BAS) in contact with the solution in the channel. On the nanotube chip

there is a gold working electrode which is used to gate the solution. The reference electrode is used to measure V_g. For small gating voltages (typically ranging from -500 mV to 200 mV) the reference electrode can be used as both the working electrode and reference electrode with minimal error.[64] Faradaic currents are monitored during the experiment and never exceed 1 nA. A typical Faradaic current measurement is shown in Fig. 3.15.

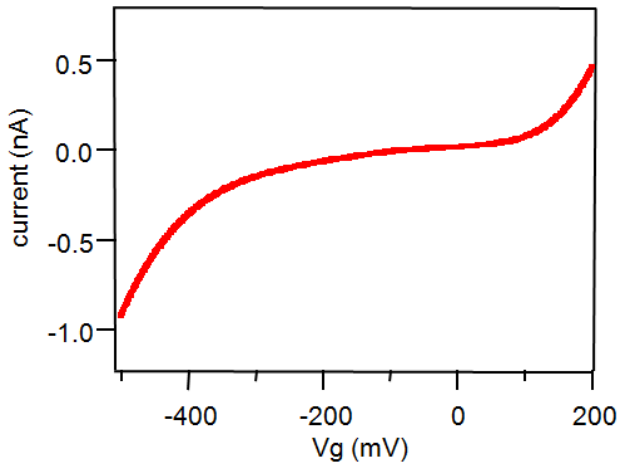

Figure 3.15 Faradaic Current. A typical Faradaic current measurement of a gold electrode CNT FET in a microfluidic environment.

There are some downsides to using PDMS.[65] One problem is that the PDMS is permeable to water and small molecules, so there is leaching in and out of the side walls of the channels. This is bad because it could introduce contaminants into the solution, either from a previous solution that has been through the channel or some uncured polymer left from the fabrication process. In our experiments the PDMS is first flushed with hexane, IPA, the DI to remove any loose polymer left in the PDMS. PDMS will easily absorb hexane and will swell to twice its initial size. The hexane, IPA, and DI

flushes out the stamp and minimizes the amount of contaminants that will leach out during an experiment. Also sensor surfaces that have been in contact with PDMS are compromised for reuse. It can be observed by eye that the area touched by the stamp is more hydrophobic than the untouched surface. This hydrophobic surface remains even after the chip has been through a cleaning anneal.

The issues of PDMS contamination has been an active area of research. For example, it was recently shown by Marie et al. that PDMS channels can be treated with PLL-g-PEG to limit nonspecific binding to channel, which limits the amount of contamination on the sensors from leaching.[66,67]

PDMS microchannels are a simple way to provide fluid integration with microelectronics. Some advantages include simple fabrication of the PDMS stamp and simple attachment of the stamp to the microelectronics. Our channels provide well controlled fluid environments, where fluid flow is easy to model. The main downside of PDMS is its permeability, but it is still useful a research tool.

3.3.2 Sensor response time and calibration

When delivering solution to the sensor, the lead volume must be flushed. The lead volume is the space in between the new solution and the sensor. A pH detection experiment was designed to find the lag time to reach fully-developed flow after solutions are switched.

Figure 3.16 shows that the pH sensing signal takes 30 – 60 sec to develop when using a pressure-driven flow rate of 170 μl/min. For slower flow rates (17 μl/min) the

signal settles in 100 – 200 sec. This lag time is a function of the length and cross-section of the piping in the microfluidics and the diffusion constant of the molecule being delivered to the sensor. Fast flow rates are desirable for minimizing the lead time, however, high flow rates use more sample volume and potentially create systematic sensing errors. For example, high flow rates are known to change the electrostatic potential at the sensor surface, thereby interfering with the sensing of charged proteins.[68]

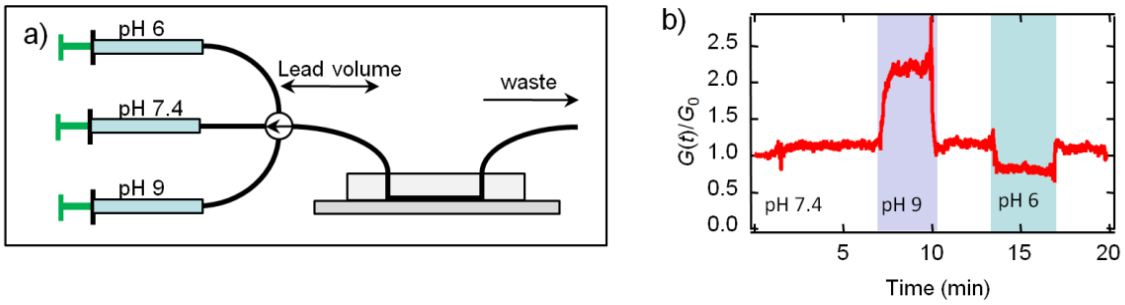

Fig. 3.16 pH calibration on a CNT circuit. a) Diagram of our microfluidic system showing 3 syringes with solutions of PBS at differing pH. A microfluidic hub (Upchurch Scientific, dead volume 12 μl) switches between different syringes. The lead volume of tubing is 6 μl (15 cm length, 225 μm inner diameter) and the lead volume in the PDMS is 6 μl. b) Plot of nanotube conductance as the pH of PBS buffer is changed. A constant flow rate of 170 μl/min is controlled by a syringe pump.

This style of pH sensing experiment gives a lower limit of the lag-time for proteins to begin binding to a biosensor. Protons diffuse rapidly across flow lines and will reach the sensor surface faster than proteins. A spherical protein with a mass of 50 kDa has $D \sim 10^{-10}\ m^2 s^{-1}$ .The diffusion constants can be estimated from the Einstein relation $D = k_B T/6\pi\eta r$, where k_B is the Boltzman constant, T is temperature, η is the viscosity of water, and r is the protein radius which we estimate by assuming spherical geometry and

protein density 1.2 x 10^3 kg/m^3. Thus, the typical diffusion constant of a protein in solution is 100 times less than the diffusion constant of a proton in solution.

Figure 3.17 shows the effective change in gate voltage ΔV_g when pH is changed. The function $G(V_g)$ shown in Fig. 3.17a was used to convert $G(t)$ data from Figure 3.16b into $\Delta V_g(t)$. Changing the pH of the solution causes changes in the charge density at the SiO_2-water interface. When pH is increased to 9, the surface loses protons and ΔV_g is negative. When pH is decreased, the surface is protonated and ΔV_g is positive. These measurements are a useful calibration of the performance of the charge-sensitive biosensor. The theoretical maximum change in surface potential for SiO_2 is 60 mV/pH.[69] Figure 3.17b shows a change of roughly 40mV/pH, and we have observed a range of sensitivities from 10-50 mV/pH. Variability may be due to organic residues on the SiO_2 surface or variability in CNT diameters.

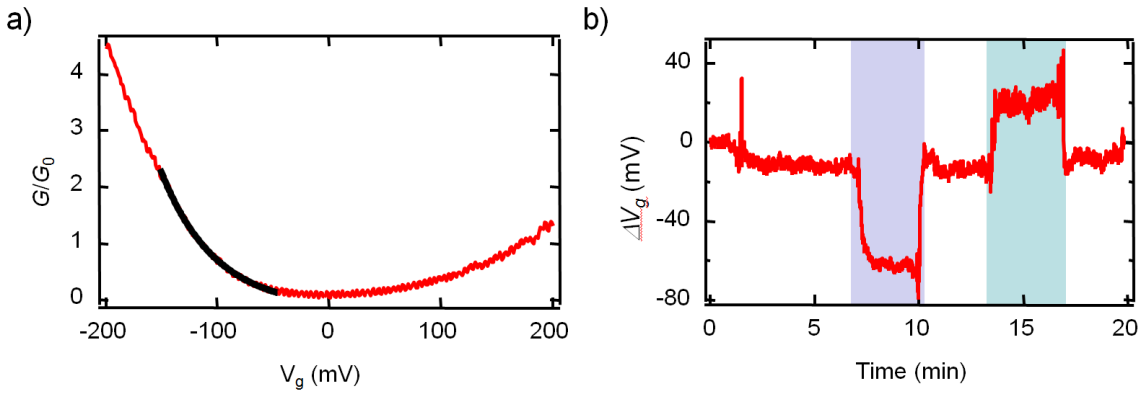

Figure 3.17 6a) Transistor curve of the nanotube circuit from Figure 3.15, the black line is fit to the curve and is used to extrapolate the effective shift in gate voltage ΔV_g that is caused by changes in pH. The bulk solution potential V_g is set to -115 mV during the experiment. b) Plot of the shift in potential ΔV_g. The shift is zero at pH 7.4 and changes by 46 mV when changing to pH 9, and changes by 36 mV when changing to pH 6.

This style of pH experiment identifies a lower bound for the shortest possible detection time and gives us insight into the timescales we should expect for other biosensors. It also quantifies the coupling between surface charge and the conductance of our CNT FET sensors.

CHAPTER 4

INCREASING PROTEIN FLUX BY LIMITING BINDING LENGTH

Detection time is a critical issue for nanoFET biosensors.[41,42] After introducing an analyte solution to a sensor, convective, diffusive and reactive processes can take tens of minutes or longer to fill binding sites on the sensor surface. Detection time depends both on these mass transport limitations, and on the biosensor signal-to-noise ratio. Previous work has focused on building nanoFET sensors with high signal-to-noise ratios,[11,70,71] but there has been almost no optimization, or even quantification, of the rate that molecules bind to the sensor surface. Notable nano-FET experiments[25] have not yet been reconciled with mass-transport modeling, despite significant modeling efforts.[42]

In this work we quantify the binding rate of protein to a CNT FET biosensor and verify that our measurements are consistent with mass transport modeling. We show that these bindings rate can be increased by modifying the design of the biosensor and demonstrate a 2.6 fold improvement in response time.

4.1 Poly-L-Lysine

We have chosen poly-L-lysine (PLL) as a model protein for investigating mass transport to CNT FET sensors. The poly-L-lysine (FITC-labeled PLL, molecular weight 25 kDa, net charge $q_{PLL} \sim 170e$, NANOCS) is fluorescently labeled to allow independent fluorescence-based measurements. The diffusion constant of PLL with this molecular weight is $D = 4 \times 10^{-13}$ $m^2 s^{-1}$.[72]

Poly-L-lysine is a positively charged protein (one positive charge per monomer at neutral pH) and has a strong affinity to bind onto the negatively charged SiO_2 substrate of our devices. All experiments were carried out in phosphate buffered saline (PBS) with pH = 7.4. In these conditions, the SiO_2 surface has a charge density of approximately σ = -2.5 $\mu C/cm^2$.[36] The net charge of the SiO_2 surface is reduced as PLL binds to the oxide. Previous work has shown that CNT FET devices can report changes in the net surface charge at a SiO_2-liquid interface.[36]

4.2Fluorescent experiments

Figure 4.1a shows the gate-response of a CNT FET before and after exposure to PLL. The gate voltage, V_g, is applied to the ionic buffer via the Ag/AgCl reference electrode. The conductance of the CNT FET increases as the semiconducting CNTs are doped p-type (more negative V_g) and n-type (more positive V_g). After PLL binding, the whole transistor curve shifts to the negative V_g direction by an amount ΔV_g = -50 mV.

To confirm that polylysine had bound to the surface of the nanoFET, the device was rinsed, dried and then imaged in a fluorescence microscope. Fig. 4.1b shows a collection of data from several sensing experiments on different sensor chips. Each data point represents a two-step experiment where first ΔV_g was recorded in the microfluidic environment, and second, fluorescence intensity was determined using a fluorescence microscope.

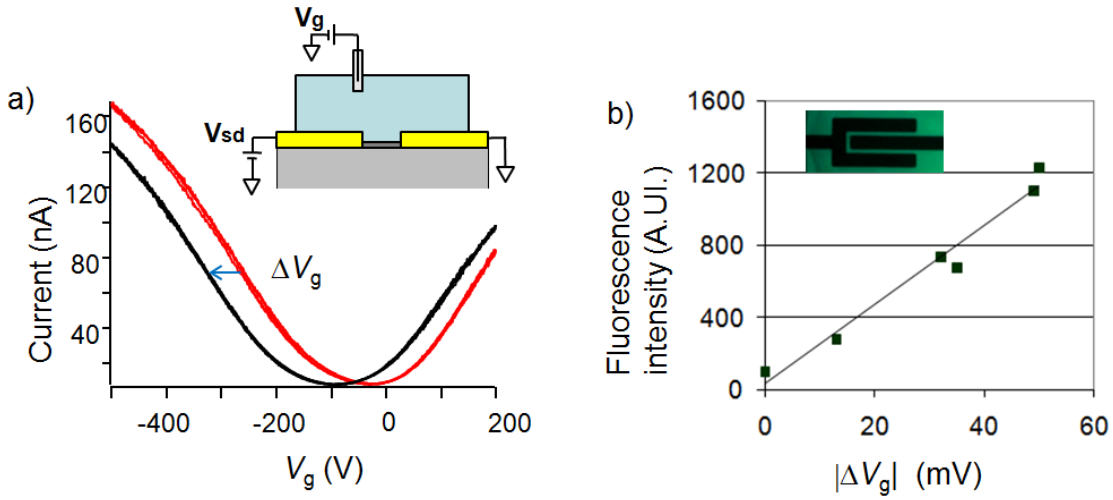

Fig 4.1 Correlation of fluorescence to ΔV_g a**)** Transistor curves measured in the microfluidic environment before and after exposure to PLL. Polylysine (positively charged) causes the curve to shift in the negative V_g direction. The horizontal shift in the $I(V_g)$ curve is labeled ΔV_g. The inset shows the experiment geometry. **b)** Fluorescence counts per unit area are compared to ΔV_g. The data point at $\Delta V_g = 0$ corresponds to background fluorescence before a binding experiment. The inset shows a typical fluorescence microscopy image (70 x 140 μm field of view) that was used to independently quantify the binding of PLL (green fluorescent label) to the oxide surface.

We interpret $\Delta V_g < 0$ as n-doping of the CNT transistor due to a blanket of positively-charged PLL coating the SiO_2 substrate. The functions $I_{initial}(V_g)$ and $I_{final}(V_g)$ are identical except for a linear shift, i.e. $I_{final}(V_g) = I_{initial}(V_g - \Delta V_g)$. This behavior is consistent with purely electrostatic doping of the semiconducting CNTs; there is no evidence for a change in carrier mobility, gate capacitance or metal-CNT contact resistance.[37] The magnitude of the shift ΔV_g is consistent with previous work,[36] and theoretical estimates made in section 4.6.

Figure 4.1b shows a linear correlation between ΔV_g and fluorescent intensity. Since florescence intensity is proportional to the total amount of bound protein,[17] we conclude that the surface concentration of bound PLL is given by

$$b \approx \left(\frac{\Delta V_g}{50\,\mathrm{mV}} \right) b_m \,, \tag{4.1}$$

where b_m is the surface concentration of available binding site. We can estimate b_m from the SiO_2 surface charge density and the PLL charge, i.e. $b_m \sim \sigma_{oxide}/q_{PLL} = 10^{11}$ cm^{-2}. The actual value of b_m may be somewhat higher because charged polymers are known to overcharge a surface before all binding sites are filled.[62]

We did a second experiment similar to Figure 4.1b but stepwise on a single chip, instead of a collection from many chips. The experiment is shown in fig. 4.2. This produced a very linear correlation between fluorescent intensity and ΔV_g. The first 3 points are taken sequentially in the same day. Fluorescence was measured within hours of binding. The last point was taken the day after, the fluorophore sat on the chip 24 hrs before imaging. Notice that the last point has a lower intensity than the previous. This may be due to the bleaching of the fluorescent tag, and over saturation of the chip where part of the potential shift is caused by proteins that are only weakly bound and eventually rinsed off.

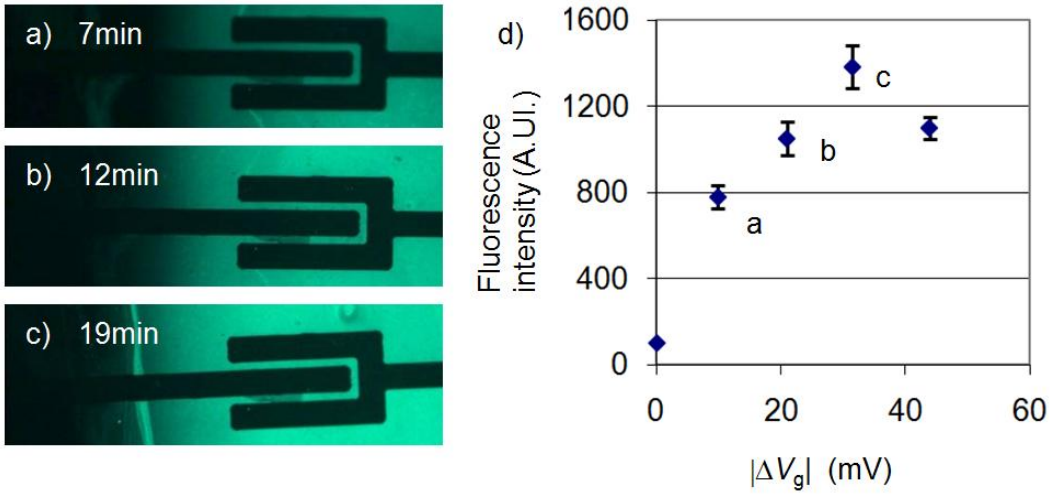

Fig. 4.2 Single Chip fluorescence correlation. a), b) and c) are fluorescence images of a single CNT sensor after exposure to poly-L-lysine for 7, 12, and 19min respectively. d) Graph of the measured change in V_g and the flourescent intensity. ΔV_g was measured in 4 steps where each recorded change is added to the last. The graph shows a linear response up until the last point where the fluorescence drops. This may be due to the overnight delay between meausrements and issues with the sensor being close to saturated.

Our fluorescence experiments show that ΔV_g is linearly proportional to the amount of bound PLL on the sensor. Since fluorescence microscopy is a well established method of quantifying proteins we can say with confidence that ΔV_g is proportional to bound protein as long as pH and other variables are held constant.

4.3 PLL Binding Rate

Figure 4.3 shows a real-time sensing experiment using two different concentrations of PLL. The signal $\Delta V_g(t)$ was inferred from a real-time measurement of $I(t)$ at constant V_g. Transistor response curves ($I(V_g)$ measured before and after PLL binding) were used to convert $I(t)$ to $\Delta V_g(t)$. The channel was first flushed with PBS for 10 min to check the stability of the device conductance. At $t = 0$, low concentration PLL

(C_0 = 4 nM) was added and we observed $d\Delta V_g/dt$ = 1.9 mV/min. At t = 7 min, high concentration PLL (C_0 = 44 nM) was added and we observed $d\Delta V_g/dt$ = 15.2 mV/min, an 8-fold increase. The signal saturates at $\Delta V_g \approx 50$ mV.

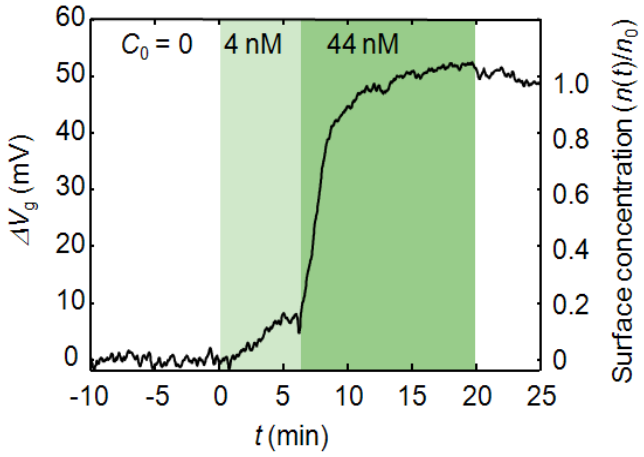

Fig. 4.3 Flux of protein for different analyte concentrations C_0. A 10 minute baseline curve is first established in PBS (C_0 = 0). At t = 0, PLL (4 nM in PBS) is added and ΔV_g changes at 2 mVmin^{-1}. At t = 7 minute, 44 nM polylysine is added and ΔV_g changes at 15 mVmin^{-1} before saturating at 50 mV. At t = 20 minutes the chip is rinsed with PBS. The flow rate is 33 μl/min for the entire experiment.

To understand the dependence of concentration on protein flux $d\Delta V_g/dt$, we consider the convective and diffusive processes transporting PLL within the microchannel. Figure 4.4a shows the steady-state concentration of PLL above the CNT FET sensor predicted by finite element computations of protein mass transport. The model assumes that protein binding kinetics are instantaneous compared to transport to the surface. The interplay between diffusive transport (random motion of PLL) and convective transport (PLL swept downstream by the fluid flow) leads to a depletion zone above the sensor of thickness δ.[42]

$$\delta = \left(\frac{DH^2 WL}{Q} \right)^{1/3} \tag{4.2}$$

Where L is the length that binding sites extend upstream of the sensor, H is the height of the channel, W is the width, and Q is the volumetric flow rate. For our channel dimensions and flow rate (W = 200 μm, H = 100 μm, Q = 33 μl/min, L = 1 cm), Eqn. 4.2 gives a depletion length δ = 1.3 μm. The steady-state flux of PLL to the oxide surface is then

$$j_D \approx D\frac{dC}{dz} \approx \frac{DC_o}{\delta}. \tag{4.3}$$

In the case that binding kinetics are instantaneous compared to diffusive transport, $j_D = db/dt$. From Eqn. 4.2 we predict that db/dt is linearly proportional to concentration, in agreement with our observations. Moreover, when C_0 = 4 nM, Eq. 2 predicts $db/dt \approx 5 \times 10^9$ cm^{-2} min^{-1} = $0.04 b_m$ min^{-1}, where the second equality follows if $b_m = 1.3 \times 10^{11}$ cm^{-2}. This rate of protein binding is equivalent to the measured value $d\Delta V_g/dt$ = 1.9 mV/min (see Eqn. 4.1).

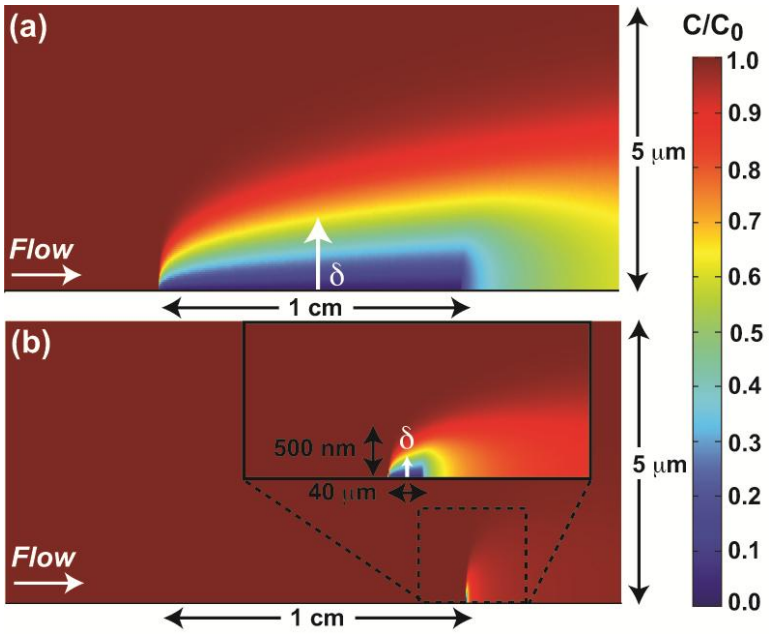

Fig. 4.4 Finite element computations of protein concentration. We compute the concentration along the length of the microfluidic channel, up to a height 5 μm above the surface. **a)** The standard biosensor design has PLL binding sites extending L = 1 cm upstream of the biosensor. The resulting depletion zone has a height $\delta \approx 1.3$ μm. **b)** The modified biosensor design has PLL binding sites extending only L = 40 μm upstream of the biosensor. The resulting depletion zone has a height $\delta \approx 200$ nm. Both steady-state computations are performed in the mass transport limit, which assumes that binding kinetics are instantaneous compared to protein transport to the sensor. Image courtesy of Todd Squires and Robert Messinger

We have repeated experiments similar to the one shown in Fig. 4.3 many times at varying concentrations and a summary is shown in Fig. 4.5. There is some spread in the value of $d\Delta V_g/dt$ for a given concentration, but there is a clear trend of increasing $d\Delta V_g/dt$ with increasing concentration, which is expected from equation 4.3.

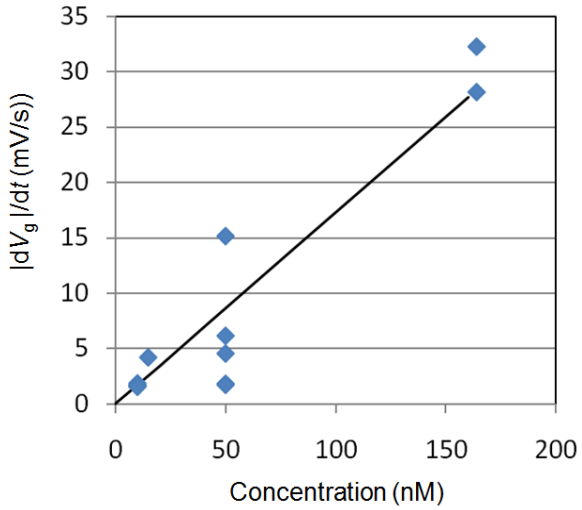

Fig 4.5 Protein flux as a function PLL concentration. The blue dots represent 11 individual CNT biosensor experiments measuring the protein PLL. Each experiment has an associated rate of ΔV_g and concentration of PLL. The line is an empirical ideal rate based on the average of 5 independent 10nM rate experiments. There are 3 points from experiments using 110kD and the concentration was multiplied by $(110kD/25kD)^{1/3}$ to account for the change in mass and diffusion constant.

The experiments in Figs. 4.3 and 4.5 show that $d\Delta V_g/dt$ is proportional to concentration as predicted in Eqn. 4.3 We have also shown that the theoretical flux of protein is in quantitative agreement with the measured ΔV_g of our CNT biosensors.

4.4 PolyEthylene Glycol coatings

To decrease the detection time of the biosensor, we have manipulated the length of the upstream binding regions to achieve an increased flux of PLL to the surface. The sensor was otherwise identical to the other devices used, but has a protein repellent polyethylene glycol (PEG) coating applied to the bare SiO_2 surface upstream of the sensor [73] In this modified biosensor, the length of the upstream binding sites is reduced from L = 1 cm to 40 μm, which decreases the depletion length δ, and therefore increases

the protein flux j_D to the sensor (Fig. 4b). After PEG deposition, $\delta \approx 200$ nm, compared to $\delta \approx 1.3$ μm for an unmodified CNT biosensor.

We now determine the fundamental limits on flux enhancement possible with this strategy. The upper bound for flux enhancement occurs in the 'mass transport limited' regime, where protein binding kinetics are instantaneous compared to transport to the sensor. In this case, the maximum flux increase for this CNT biosensor can be calculated analytically, yielding a device-specific enhancement of 8.3 upon PEG deposition. The lower bound occurs in a 'reaction limited' regime, where binding kinetics are slow compared to transport, so that the protein concentration C_0 is uniform throughout the microfluidic channel. In this case, no flux enhancement occurs. Thus, the CNT biosensor would operate completely independently of the upstream SiO_2 binding region.

The PEG-modified devices were created as follows. Carbon nanotube FET chips were patterned by photolithography and then soaked overnight in an aqueous pH 2 solution of HCl and 2% 2-[methoxy(polyethyleneoxy)-propyl]9-12trimethoxysilane (Gelest). The chip was then rinsed and then baked at 115 ºC for 30 min to ensure covalent bonding of the PEG to the oxide surface. The chip is then rinsed again with DI water before removing the photoresist in remover. An example wafer patterned with PEG and tested with PLL is shown in Fig. 4.6.

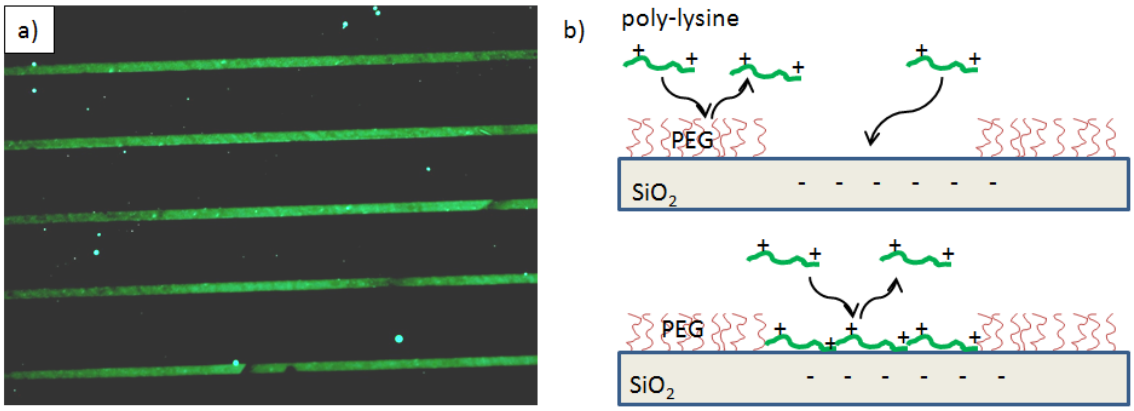

Fig. 4.6 Poly-Ethylene-Glycol patterned chip tested with fluorescent poly-L-lysine. The black areas are coated with PEG and repel the PLL from binding. The green is fluorescent PLL bound to bare silicon oxide surface b) Cartoon of the effect of PEG on a molecular level.

4.5 The Effect of PEG on Binding Rate

A comparison between a PEG-modified and a standard biosensor is shown in fig. 4.7, which is the key result of this chapter. As in Fig. 4.3, PBS buffer was flushed over the clean sensors to check device stability before adding low concentration PLL (C_0 = 4 nM). Figure 4.7a and b show fluorescence microscope images taken after the sensors were saturated with PLL. The PLL (green fluorescent label) binds to all oxide surfaces of the standard biosensors, while the PLL is localized to a small area of the PEG-modified biosensor. During real-time sensing (Fig. 4.7c) the biosensor chip reports an initial flux of $0.04 b_m$ min^{-1} (we use Eq. 1 is used to convert $d\Delta V_g/dt$ to units of b_m min^{-1}). The PEG-modified biosensor reports a faster initial flux of $0.10 b_m$ min^{-1}, resulting in a flux enhancement of 2.6. The experiment shown in Fig. 4.7 was repeated four times. In each trial, the rate of protein binding to the PEG-modified sensor was higher than the rate of

protein binding to the standard biosensor. The ratio of binding rates varied from 1.9 to 3.2, and details of the 4 experiments are shown in Table 4.1

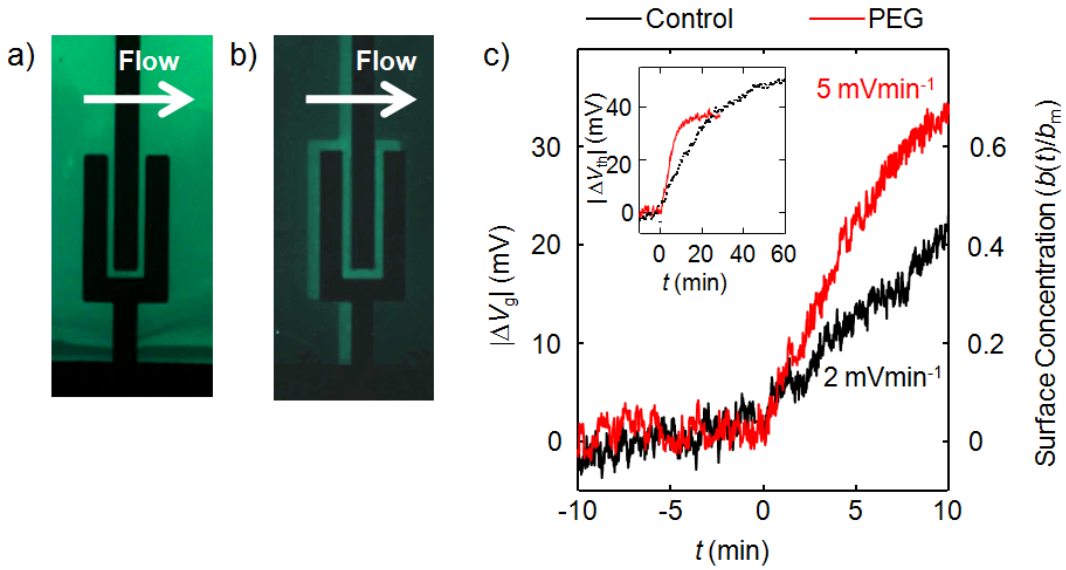

Fig. 4.7 Modified sensor geometry and accelerated PLL binding to the sensor. **a)** Fluorescence image (70 x 140 μm field of view) of PLL bound to the surface of a standard biosenor. Fluorescence intensity in the gap between the two metal electrodes is 1230 counts per pixel. **b)** Fluorescence image of PLL bound to the surface of a PEG-passivated biosensor. Fluorescence intensity in the gap between the two metal electrodes is 730 counts per pixel, fluorescence intensity on the PEGylated surface is 120 counts per pixel. **c)** Real time detection of 4 nM PLL binding using the standard sensor and PEG-modified sensor. Analyte is added at $t = 0$.

Our observed flux enhancement (2.6x) differs from the maximum possible increase (8.3x) from PEG treatment. For our CNT biosensors, two factors contribute to this behavior. First, the biosensors are not operating in the mass transport limited regime, which is required to obtain the optimal flux increase. If the sensors were mass transport limited, then the flux to the CNT sensor would be constant, which we do not observe. Thus, the device operates within an intermediate regime that is neither reaction nor mass

transport limited. Second, the PEG coating is not 100% effective at blocking PLL binding. The fluorescence microscopy image (Fig. 4.7b) shows that some PLL binds to the PEG-treated surface (the ratio of PLL on oxide to PLL on PEG is 6:1). This upstream binding partially depletes the analyte concentration before it reaches the sensor, reducing the protein flux.

Regardless, the observed 2.6-fold flux increase (db/dt) corresponds to a significant improvement in detection time. For a given signal-to-noise ratio and analyte concentration, detection time is cut in half by using the modified sensor. We note that other biosensors could potentially realize their maximum flux enhancement with this strategy, provided that (i) the sensors operate in a mass transport limited regime, and (ii) the protein repellent layer successfully inhibits adsorption of PLL to the upstream binding region.

Improving the quality of the PEG coating, by both increasing protein repellency and decreasing cross contamination during PEG patterning, remains an experimental challenge. Figure 4.7 shows that, upon saturation, more PLL was absorbed to the control device than the PEG treated device. This trend was seen in all 4 trials. We postulate that PEG which is not covalently bound to the SiO_2 is not completely washed off after the bake-on process. This loose PEG may contaminate the sensor during photoresist liftoff, or during the first half of the microfluidic experiment ($t < 0$). This cross-contamination is an important consideration for future device fabrication processes.

Table 4.1 shows 4 pairs of experiments showing the effects of limiting binding length with PEG on protein flux. The average factor of improvement in $d\Delta V_g/dt$ for the 4 experiments is 2.7. All experiments show an increase in performance when using PEG and the average improvement is consistent with our representative experiment shown in Fig. 4.7

experiment	1	2	3	4	average
Control (mV/min)	1.87	4.60	1.73	1.70	2.48
PEG (mV/min)	5.79	8.77	5.48	4.30	6.09
ratio	3.10	1.91	3.17	2.53	2.67

Table 4.1 Table of PEG experiment pairs. Each table has a pair of sensing experiments, one control with no PEG and a PEG coated chip.

The experiments in this section demonstrate that protein flux can be controlled by controlling the available binding length in the channel. We observed an improvement of $d\Delta V_g/dt$ by a factor of 2.6. This factor correlates to an increase in protein flux and a faster working biosensor. This factor can be easily improved by further shrinking the size of the binding length by designing smaller device geometries using more modern photolithography techniques.

4.6 Theoretical Estimate of ΔV_g

We can use the theory of surface potentials introduced in chapter 2 to calculate the expected change in ΔV_g when detecting our model protein poly lysine. The charge of silicon oxide in a 100 mM salt solution is approximately -2.5 μCcm^{-2}. [36] This means that there will be roughly one electron per 2.5x2.5 nm square. Polylysine has one positive charge per monomer. Two or three monomers of polylysine can fit across a 2.5 nm

square and therefore a polylysine laying flat on a silicon oxide surface will have two or three positive charges per negative charge in the silicon oxide. Assuming a charge density of 2 times the oxide charge we can use Eqns. 2.15 and 2.16 to find the potentials $\Phi_2 = 50$ mV, and $\Phi_0 = 100$ mV. Using Eqns. 2.14 and 2.16 we find the average potential around the surface of a 1 nm nanotube a value of 57 mV. This shift is consistent with the observed shifts in potential. In the situation described above the poly lysine forms much less than a monolayer to create twice the oxide charge. This means that it is reasonable to assume that the protein film is thin. Unfortunately it is difficult to know the exact surface charge and density of absorbed poly lysine so it may not be practical to get more than a first order approximation. This calculation raises the issue of CNT diameter dependence on ΔV_g. Larger CNTs will experience smaller values of ΔV_g, which creates variability in signals generated by different devices. Figure 4.8 illustrates the ΔV_g diameter dependence using the calculation described above.

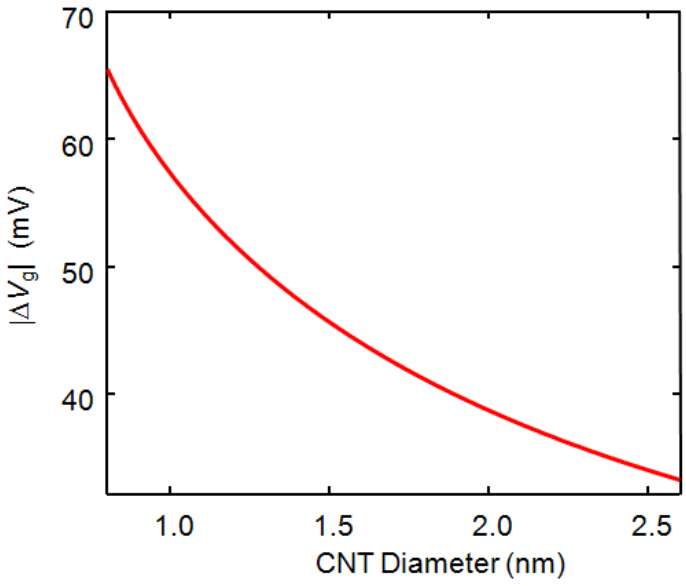

Fig. 4.8 Theoretical diameter dependence of ΔV_g caused by polylysine coating. We assume that the surface charge density changes from having a negative surface charge native to silicon oxide in a salt solution, to a positive charge density of equal value from absorbed protein. This model does not account for charged protein that lands on the surface of the tube, and is therefore an underestimate of ΔV_g for a given diameter and density of protein

4.7 Depletion of PLL Solutions

PLL has a strong affinity to bind to silicon oxide surfaces and will bind to the sides of the container that it is stored in. This problem is most significant for low concentration solutions because it can deplete a large fraction of the available protein. To address this problem most solutions of PLL were mixed in glass bottle that had already stored PLL. This meant that PLL had already saturated the container surface and was likely not to deplete the solution in a significant way. New bottles were used when a solution may have been compromised or when cleanliness was deemed especially important. The following is a fluorescence experiment that illustrates how a container can deplete a solution.

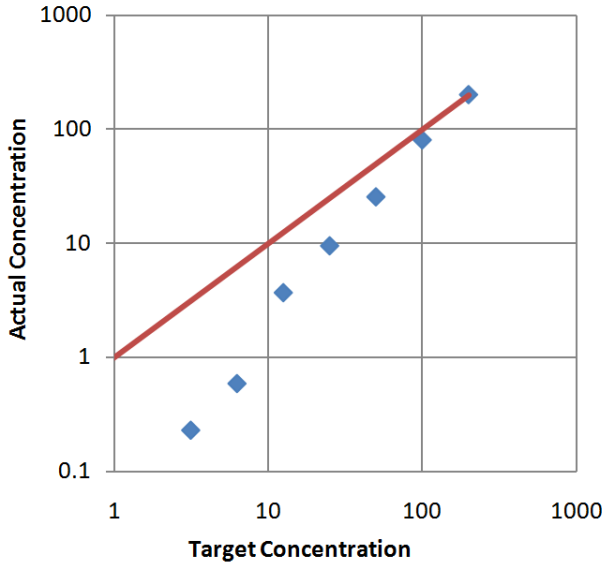

Fig. 4.9 Depletion of PLL solutions due to glass containers. Fluorescence measurements were done with a microplate array in triplicate. The solutions of PLL were mixed in fresh glass containers and allowed to sit for 30min before the fluorescence measurement was taken. Ideally the data should have a straight line with a slope of one (shown in red), but because of depletion onto the sidewalls of the container the measured concentration is lower than the ideal, especially at lower concentrations. The concentration is measured by using the fluorescent intensity relative to the highest concentration measured (200 nM)

4.8 Future Research

By using PEG we were able to increase the flux of protein onto a CNT sensor, but the improvement was less than our theoretical estimates based on the sensor geometry. Defects in the PEG coatings are a likely explanation for the discrepancy between experiment and theory. With fluorescent microscopy we observed that there is still polylysine adsorbed onto the PEGed areas and the bare SiO_2 has less poly lysine than wafers that were left untreated with PEG. Problems with ineffective PEG coating may be traced back to the oxygen plasma step in the reactive ion etch (RIE). The RIE is a multi-function machine that etches silicon oxide as well as oxygen plasma cleans. It has been

noticed that chips that have been cleaned with oxygen plasma have a residue on them right after the RIE has been used for an oxide etch. We minimized the residue by doing a chamber clean in between runs, but it is still possible that it is interfering with the effectiveness of the PEG coating. The problem of low binding on the bare SiO_2 may be caused by weakly bound PEG rinsing off and depositing onto the bare SiO_2. This problem may be helped by doing an aggressive cleaning after the covalent of binding of the PEG, but before lift-off. Boiling water may be a good choice because it is non-destructive to photoresist, but good at removing water soluble PEG.

Future researchers should be aware of the importance of substrate of the sensor. Our experiments suggest that CNT FETs on oxide surfaces act as a probe of the average surface potential. It is well known that the surface potential of an oxide is very sensitive to processing history and we have also observed such sensitivity. For example, using a CNT FET pH sensing experiments first, and a then a polylysine sensing experiment, will lead to a different saturation value of ΔVg upon polylysine binding. This is likely due to a change in the surface charge in the silicon oxide that remains even after returning to neutral pH. Our experimental protocols have been designed so that identical processing steps are used for each sensor we test. For example, devices with PEG and devices without PEG are both covered with photoresist the same number of times to make sure all sensors have comparable surface charges. Future investigations of CNT FETs built on different substrates, or CNT FET that are suspended (no substrate) would help clarify the importance of the substrate.

Issues with surface variability also raise concern about long detection experiments. Low concentration detection experiments will develop a signal very slowly and will be susceptible to drift in surface potential. The experiment shown in Fig. 4.7 had an hour long PBS rinse before beginning the experiment to ensure that the sensor had equilibrated with the aqueous environment. An example of this slow current drift is shown in Fig. 4.10. A possible solution to account for drift is to store the sensor in a buffer environment, eliminating the need for a long pre-rinse because the sensor has already equilibrated.

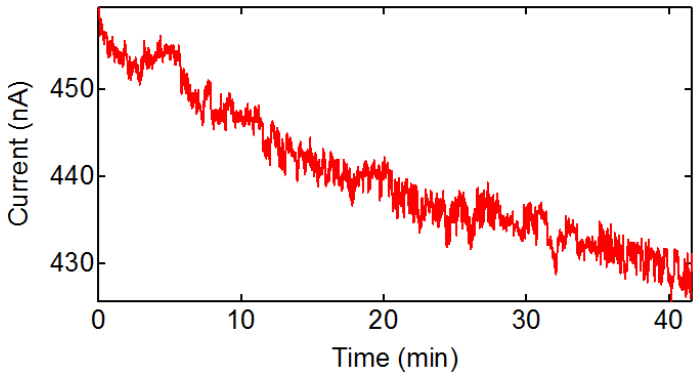

Fig. 4.10 Drift in current during a PBS rinse. When a sensor is first introduced to an aqueous environment the sensor surface will slowly equilibrate. The current drops by about 6%, or equivalently shifted by 20 mV.

4.9 Conclusions

In this chapter we discussed how for the first time protein flux onto a FET biosensor has been quantified. Quantification was done by monitoring the potential of the CNT FET during protein adsorption and with the use of fluorescent microscopy. We showed that mass-transport can be controlled by using the surface coating PEG. By decreasing the available binding length with PEG we built a faster biosensor. This is an

important step towards optimizing the design of FET biosensors. This work can be continued further by making sensors with smaller binding lengths. This can easily be achieved using modern photolithography techniques, or by shrinking the sensor to the fundamental limit by using a single suspended nanotube. If all other surfaces are covered in PEG the only available binding surface is the CNT.[74,75] A suspended CNT sensor could potentially respond 100 times faster than another FET of similar size.

CHAPTER 5

MEASUREMENT OF BIOLOGICALLY RELEVANT PROTEINS

This chapter discusses the detection and measurement of a few well studied biological proteins. These model proteins experiments are representative of the performance we expect from real world biosensor applications. Here we introduce a procedure for CNT functionalization using the molecule PBASE (1-pyrenebutanoic acid succinimidyl ester). We use this procedure for functionalizing biotin for the detection of streptavidin. Also we discuss non-specific functionalization of sensors with anti-P53 for the detection of P53.

To elucidate the behavior of CNT FET sensors we detected single stranded DNA, polylysine, and IgG. These three molecules are representative of negatively charged, positively charged, and charge neutral molecules. We show that CNT FETs are effective sensors in all cases and the observed response is in agreement with expectations.

Lastly, we discuss two methods for quantifying protein film thickness. It is useful to be able to quantify the protein film thickness and correlate thickness with biosensing experiments. Ellipsometry is a well established technique for measuring protein thickness in real time. AFM protein lithography is a technique used in our lab to measure protein films after they have dried onto a surface.

5.1 Specific Detection of Proteins

In order to make a useful biological sensor, the surface of the sensor must bind to the specific biomolecule of interest while rejecting other biomolecules. Otherwise the

sensor will bind to almost any molecule and will not provide useful information. Specific binding of single stranded DNA (SS-DNA) can be achieved by using the complementary SS-DNA.[2] Specific binding of proteins can be achieved using antibodies,[38] or aptamers[13]. Here we demonstrate the functionalization of CNT FET sensors and their use for the detection of P53 and streptavidin.

Typical functionalization schemes utilize antibodies to specifically catch target biomolecules from solution. The antibody acts as 10-15 nm spacer between the CNT and the target biomolecule. Therefore, biosensing in biological conditions ($\lambda_D \sim 1$ nm) is not practical. Some authors have solved this issue by using low salt buffers,[25,27] others have solved it by using a preconcentration step.[6] The use of low-salt buffers may denature proteins and reduce the affinity of antibody-antigen binding. Low salt concentrations can also lead to weak pH buffering, making solutions that are less stable in pH and are more prone to giving false signals. Aptamers are an alternative to antibodies that are essentially short synthetic antibodies made from single stranded DNA or RNA.[13] After the selective evolution process aptamers may be 50 bases long. This length can be minimized to 23 to 35 bases by removing the non-functional sections and will have a mass of that is typically around 10 kD.[76] The exact length will depend on the aptamer on how the DNA or RNA folds and its conformation. We can estimate the minimum length (3 nm) as the diameter of a 10 kD sphere, and the maximum length (12 nm) as 35 bases stretched out. They are an effective way to bring the antigen closer to the nanotube, but the number of available aptamers is smaller than the number antibodies and it is work intensive to create an

antigen specific aptamer. A list of existing aptamers is available at the Ellington aptamer lab database.[77]

5.1.1 Nanotube conjugation

To functionalize the carbon nanotube for specific binding we have followed a protocol developed by Chen et al.[78] Clean CNTs are incubated in a 1 mM solution of 1-pyrenebutanoic acid succinimidyl ester (PBASE, sold by Molecular Probes) in dimethylformamide (DMF). The best results were found when the nanotubes are incubated in solution directly after nanotube growth. The incubation time is 5 hours. The anchor molecule PBASE is chosen due to pyrene's ability to pi-stack on the CNT surface. The succinimidyl ester provides a handle for biomolecular conjugation. Succinimidyl ester is degraded by water and light, therefore, the DMF is dried of water using molecular sieves, and the solution is protected from light. After incubation, the chip is rinsed in dry DMF and then dried in nitrogen. A drop of 1 mM ferritin in PBS was placed on the PBASE-functionalized CNTs and incubated for 3hrs. Ferritin was chosen because it is easy to image by atomic force microscopy and the primary amines on ferritin will conjugate to the succinimidyl ester. The resulting conjugation of ferritin to CNTs is shown in Fig. 5.1. The scheme can easily be adapted to conjugate antibodies or aptamers to the CNT instead of ferritin.

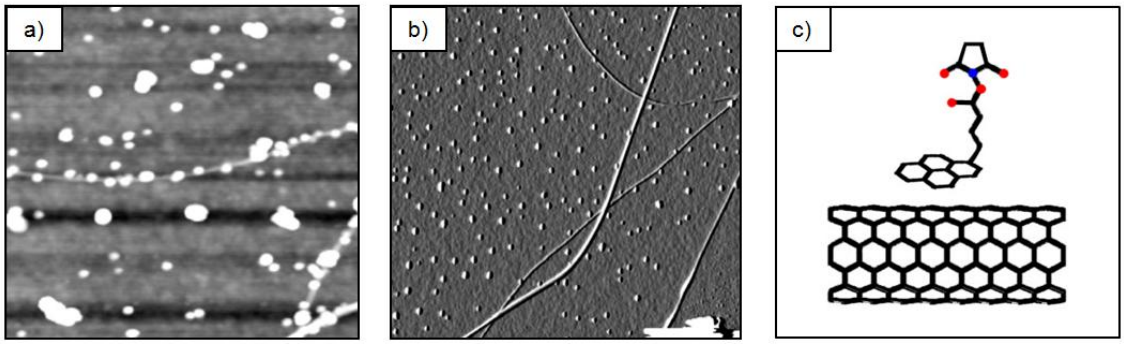

Figure 5.1 Conjugation of ferritin to CNTs. a) AFM image (1 μm x 1 μm) of CNTs (white lines) that have been treated with PBASE and then ferritin (white dots). Some ferritin complexes stick specifically to the CNT, while others stick non-specifically to the silicon oxide surface. b) AFM image (2.5 μm x 2.5 μm) Control where CNTs are not treated with PBASE before ferritin conjugation. This image shows that ferrtin does not stick strongly to the CNTs c) Schematic of the specific binding scheme. PBASE sticks to the side walls of the CNT by p stacking.

The following is an example of similar conjugation technique demonstrating specific detection between biotin and streptavidin. A solution of amino-biotin is prepared by mixing aminopyrene (sigma Aldrich) with NHS-biotin (sulfosuccinimidyl-6-(biotinamido) haxanoate, (Thermo Scientific) in DMF. A 2 mM solution of pyrene-biotin in DMF is allowed to react with CNTs on a silicon oxide surface for 1 hr. The biotin coated CNTs are then reacted for 1 hr with a solution of streptavidin coated-gold nanobeads (15-20 nm gold beads, Bio Assay Works). The nanobeads are chosen because they are large enough to be seen in an AFM. The results of this conjugation experiment are shown in Fig. 5.2

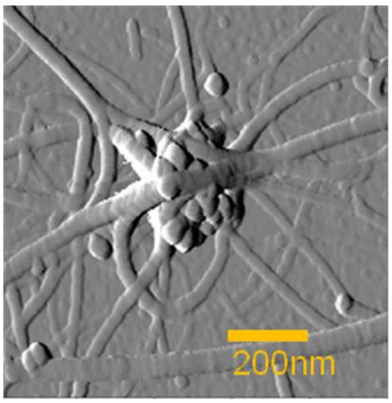

Fig. 5.2 Conjugation of streptavidin nanobeads. AFM image of streptavidin coated gold nanobeads attached to the sidewalls of CNTs using pyrene-biotin. The image shows modest success, with a significant amount of undesirable nanobead aggregation.

Pyrene has been demonstrated as an effective way to functionalize carbon nanotubes as shown in Fig. 5.1. There are still challenges that we have not addressed, such as non-specific binding of proteins to silicon oxide surfaces, and non-specific aggregation of protein. This issues need to be solved before a useful biosensor can be made, otherwise the nonspecific binding will generate stray signals on the sensor.

5.1.2 Specific Detection of the Protein P53

P53 is a cancer biomarker.[79] In the following experiment a mouse is treated with UV light to cause elevated levels of P53. There is also a control mouse not treated with UV light and should not have high levels of P53. Blood serum is extracted from each mouse to be used in a CNT FET P53 sensor experiment. The CNT FET sensor is first flushed with a solution of 10 μg/ml of anti-P53. The binding of anti-P53 is shown in figure 5.5(a and b), from this data it is clear that anti-P53 is adhered to the surface. The sensor is rinsed with buffer and then a 100 ng/ml solution from the control mouse is

added followed by a 100 ng/ml solution from the UV irradiated mouse is added. This is repeated at 1 μg/ml and 10 μg/ml concentrations. Figure 5.5c shows that that the sensor responds upon the addition of 10 μg/ml control solution. This shows that proteins will bind nonspecifically to the sensor surface despite being treated with anti-P53. In order to make a useful biosensor that can be used without pre-concentration of P53 a method must be developed to deal with nonspecific binding.

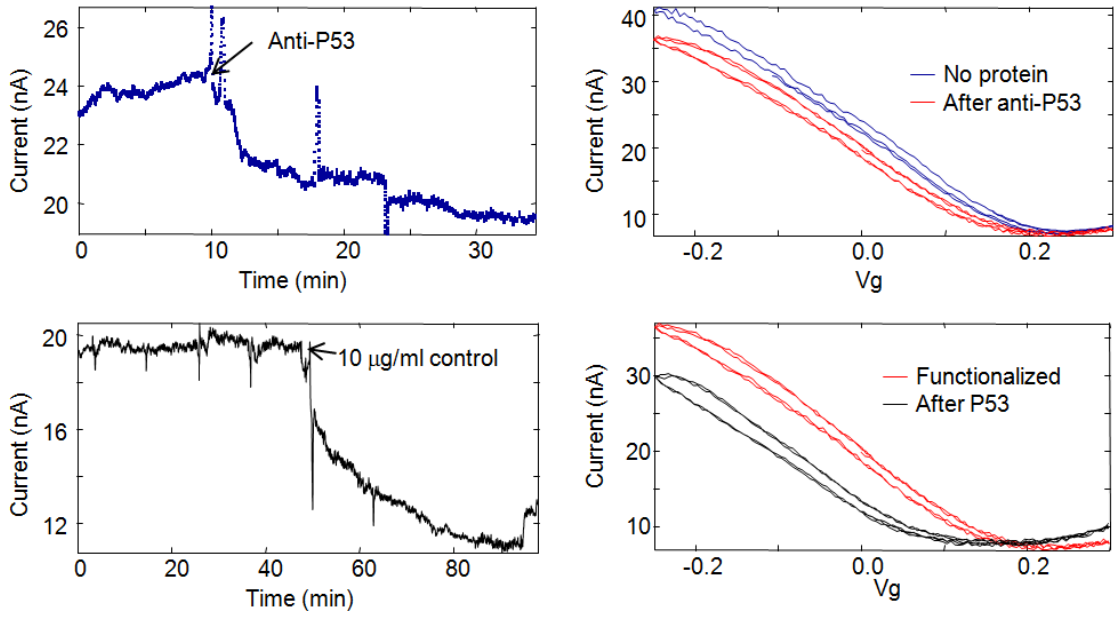

Fig. 5.3 Specific detection experiment of the protein P53. a) Real time detection of the anti body coating the CNT b) Gate voltage curves before and after the addition of anti-P53. The shift is approximately 35 mV c) Real time detection of 2 solutions, a control solution from a normal mouse, and a solution from a mouse irradiated with UV light. The concentration of the added solution is increased sequentially from 100 ng/ml, 1 μg/ml, to 10 μg/ml for both solutions. At a given concentration the control is added first followed by the UV irradiated mouse solution. There is a spike in current every time a new solution is added. Ultimately the experiment shows a large response from the control mouse at 10 mg/ml, showing that simply coating the sensor with anit-P53 is not sufficient to prevent nonspecific binding. d) Gate voltage curves before and after the addition of the mouse solutions. The total shift in threshold voltage is around 90 mV.

5.1.3 Specific Detection of Streptavidin

A good choice for preliminary biosensor detection experiments is the protein streptavidin. Streptavidin has a very high affinity to biotin (vitamin B7),[80] making it very unlikely for streptavidin to wash off once bound to the biotin on the sensor. Biotin is a very short molecule, which will allow for streptavidin to be brought close to the sensor surface producing a large electrical signal. The experiment shown in Fig. 5.4 uses a sensor treated with biotin using the procedure outlined in section 5.1.1.

In this experiment streptavidin is flushed over the sensor sequentially at concentrations of 1 nM, 50 nM, and 1 μM and then rinsed. This experiment shows the detection of streptavidin, but it does not demonstrate specific binding of streptavidin to biotin because the sensor was never challenged with another protein.

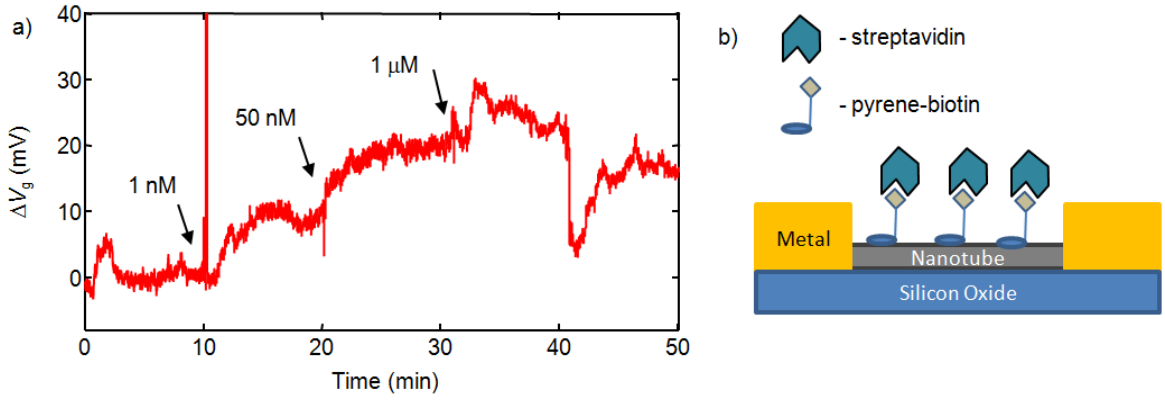

Fig. 5.4 Streptavidin sensing experiment. This sensor was first treated with biotin as outlined in section 5.1 to prepare it for a specific streptavidin sensing experiment. The sensor is first rinsed with buffer (1:100 dilution PBS in DI water). Then the sensor is flushed with 1 nM streptavidin in buffer and is allowed to saturate the sensor (8 mV shift). This is followed by a 50 nM solution (11 mV shift) and then a 1 μm solution (4 mV shift). The last step is a rinse with buffer which appeared to remove some absorbed protein (-7 mV).

This experiment uses diluted PBS in DI water to lower the salt concentration and increase the screening length and the electrical signal from the binding of streptavidin. Simply diluting PBS is not recommended for creating a low salt buffer, and this procedure allowed for significant variations in pH and caused errors in later experiments. A better procedure is to mix up a solution of phosphate buffer and adjust the pH by adding HCL. This way there is a minimum amount of salt for a given concentration of buffer and pH, while PBS has more salt for a given concentration of phosphate.

Figures 5.3 and 5.4 demonstrate the detection of proteins on functionalized CNT FET sensors. These experiments show that the sensors are sensitive enough to detect proteins even though they are separated by a functionalization molecule. Unfortunately biofouling and nonspecific binding are still problems that have not been addressed. We have yet to demonstrate an effective specific binding experiment that has been challenged with non-specific proteins.

5.2 Non-Specific Detection of Model proteins

In this section we discuss the detection of the molecules of different charge. We use the examples of poly lysine, single stranded DNA (SS-DNA), polylysine, and immunoglobulin G (IgG). We compare negatively charged SS-DNA detection to the detection of positively charged polylysine and show that they produce an opposite change in the sign of ΔV_g. We use IgG because it has a neutral isoelectric point,[81] and therefore demonstrates how CNT FET sensors are effective with neutral molecules. Also, IgG acts

as a model anti-body and shows how we can expect CNT FETs to behave as they are functionalized.

5.2.1 Effect of Charge on Sensor Potential and DNA Sensing

Single stranded DNA is a good model protein for biosensing experiments.[82,83] It can be used as a conjugate pair for testing specific detection, and DNA can be designed to have one negative charge per monomer. Figure 5.5 shows two example sensing experiments that use biological molecules of different charge: polylysine (one positive charge per monomer at pH 7.4) and SS-DNA (one negative charge per monomer at pH 7.4). From Figure 5.5 we see that polylysine binding is equivalent to a shift in gate voltage ΔV_g = +55 mV and SS-DNA binding is equivalent to ΔV_g = -45 mV. We attribute sign of ΔV_g to the polarity of the biological molecules. Differences in the magnitude of ΔV_g are likely related to differences in binding geometry and variations from circuit to circuit. Fluorescence imaging (Fig 4.2) reveals that polylysine binds to all bare silicon oxide surfaces. This binding is driven by the Coulomb interaction between negatively charged SiO2 (-2.5 $\mu C/m^2$)[25] and positively charged polylysine. In contrast, previous studies of SS-DNA show that the SS-DNA only binds to the CNT and not the SiO_2.[83]

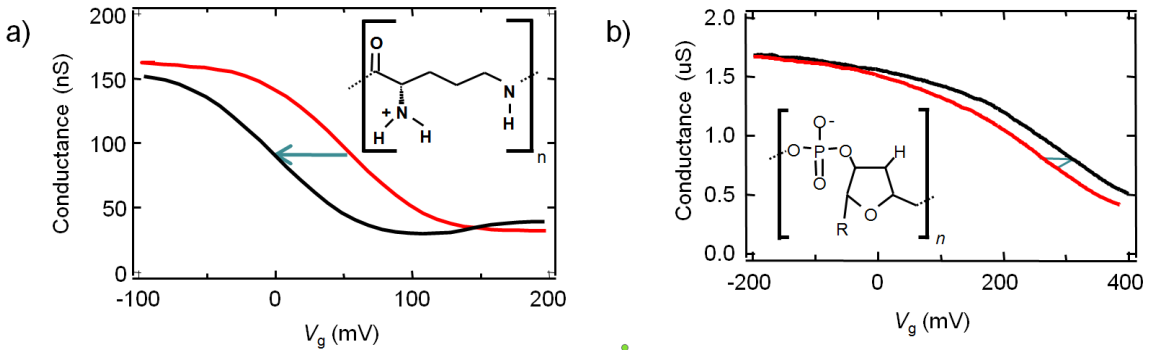

Figure 5.5 Charge dependent protein gating. a) This is transistor curve from a Poly-L-lysine sensing experiment. The red line is the nanotube transistor curve before the addition of poly lysine. The black curve is after the addition of polylysine. Notice that the curve shifts by about -50 mV. The shift is in the negative direction because polylysine is a positively charged protein. b) This is a transistor curve before (red) and after (black) the addition of DNA. Notice that the curve shifts by about 50 mV. This is in the positive direction because the DNA has a negatively charged backbone.

5.2.2 Detection of IgG

Rabbit IgG (from Thermo Scientific) is an antibody that will bind to goat IgG and is used as our model antibody. Fig 5.6 shows the non-specific detection of IgG. Unlike positively charged poly lysine or our negatively charged SS-DNA, IgG is a neutral molecule but it will still bind to the sensor surface and will still generate an electrical signal. The change generated is possibly caused by asymmetries in charge distribution or changes in the gate capacitance of the nanotube. Studies using poly electrolyte films have shown that the change in V_g can be independent of the charge of the molecule.[36] They attribute this anomalous change to a reduction in the effective screening (capacitance), because of the film of protein over the nanotube.[36] In Fig. 5.6 we observe a shift that is consistent with electrostatic doping, and has no observable change in capacitive.

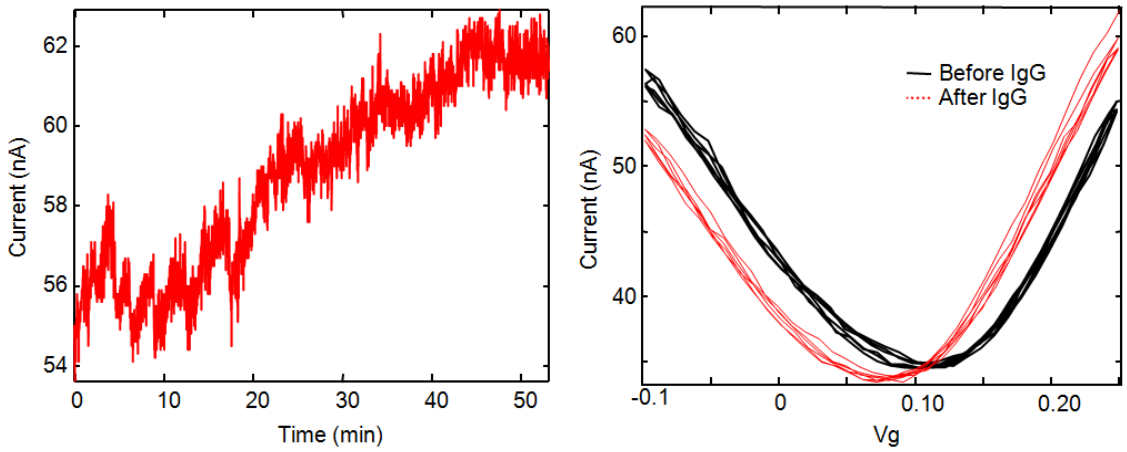

Fig. 5.6 Detection of 15 nM IgG with no flow. This detection corresponds roughly to a 30 mV shift in potential and demonstrates that a CNT FET can be effective for detecting a charge neutral molecule.

5.3 Quantifying Protein Film Thickness

Ellipsometry and AFM lithography are ways of measuring protein film thickness. They are useful tools for correlating absorption of protein onto a surface and electrical measurements from CNT FET biosensors, which is important for determining capacitive effects on FET sensors. Ellipsometry measures film thickness on a fast enough time scale to give useful information on protein kinetics and can be used to corroborate measurements from CNT FETs.

5.3.1 Ellipsometry

Ellipsometry is an established optical technique for measuring the absorbed film thickness of proteins.[84] Below are two example ellipsometry experiments with IgG and lysozyme. Unfortunately ellipsometry did not work well with polylysine because it forms layers too thin to be measured by our ellipsometry equipment.

Lysozyme is a globular protein that was chosen as a model protein because it has well known and predictable behavior. Assuming a spherical protein with a molecular weight of 15 kDa and density $1.2x10^3$ kg/m^3 we can expect a diameter of lysozyme to be 5 nm, which is larger than the observed change of 2 nm shown in Fig. 5.4. This suggests sub monolayer coverage of lysozyme.

The antibody IgG has a molecular weight of 150 kDa and is about 10nm in length[85]. Fig 5.4 shows the formation of a film 11 nm thick, which is consistent with the expected thickness.

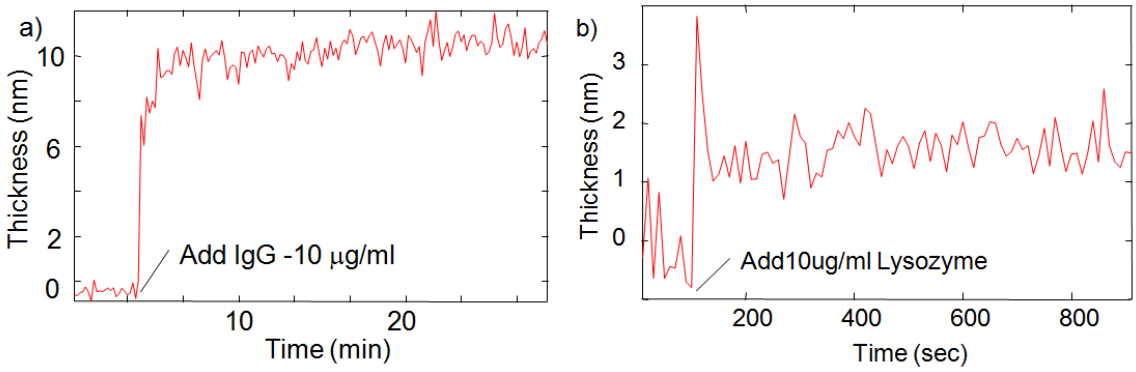

Fig. 5.7 Real time ellipsometry measurements of absorbed protein. a) Measurement of the film thickness of IgG on a silicon oxide surface. IgG has a molecular weight of 150 kDa and has a length of about 10 nm, the measured thickness is 11 nm and is consistent with the length expected value. b) Measurement of a film of lysozyme on a silicon oxide surface. We assume a diameter of lysozyme of 5 nm and observed a thickness change of 2 nm.

5.3.2 Atomic Force Microscope lithography

The Atomic Force Microscope (AFM) is often a useful tool for force probe based imaging of CNTs and CNT circuits. The AFM can also be used to quantify films of protein measured with CNT sensors. To measure the film thickness, pressure is applied to

the surface using the probe tip and the tip is dragged across, cutting a trench in the surface. This is analogous to a snow plow cutting a trench in snow. Just like a snow plow the AFM tip will often leave a large pile of protein at the end of its path. After the tip has finished dragging across the surface, it can be used to measure the profile and determine the film thickness. Figure 5.8 shows AFM images of the anti body IgG on a CNT chip. The AFM can write any desired pattern into the protein surface, for example the letters OSU. Notice in this image there are high points on the edges and end of the letters created from the pile up of displaced proteins.. We can compare figure 5.7 to 5.8c and see that the AFM measurement gives a thinner film measurement, likely because the film has been allowed to dry.

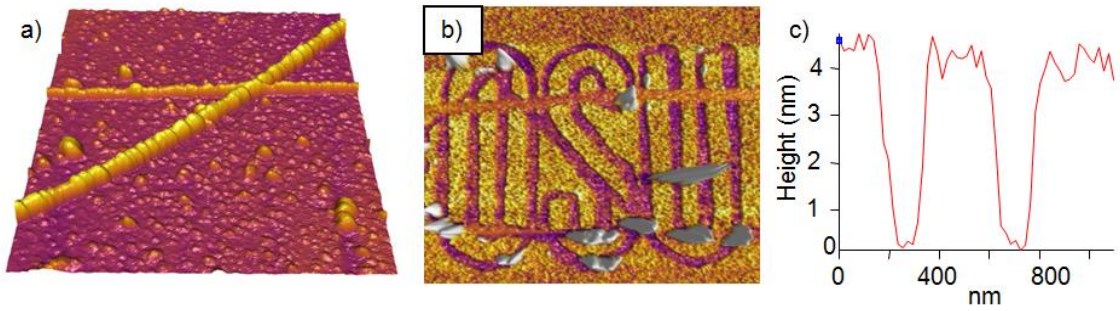

Fig. 5.8 AFM Lithography in a protein film. All three images use 1mg/ml IgG on a silicon oxide surface. a) An AFM image 1 μm wide of a carbon nanotube after IgG coating b) The IgG coating can be scratched with the AFM tip. This image shows the letters OSU drawn into the IgG film using the AFM lithography software. The image is 10 μm wide. C) Cross section of the last 2 line segments of the U show that the dried protein film is about 5 nm thick.

Protein film measurement can be a useful supplement to CNT FET data and can give insight into the FETs behavior. Ellipsometry is a useful tool for measuring average film thickness of proteins, and is capable of measuring protein absorption kinetics. The

local protein thickness around a CNT FET can be measured with AFM lithography, and can give information not revealed by average thickness measurements like ellipsometry.

5.4 Conclusion

In this chapter we showed how a CNT FET sensor can be functionalized using the anchor molecule pyrene. Experiments with pyrene showed an increased affinity of proteins to CNT surfaces. Using negatively charged DNA and positively charged poly lysine we demonstrated that CNT FETs are charge sensitive and respond in a predictable way. Experiments with the charge neutral IgG show that FET can also detect proteins that are not highly charged. We demonstrated the measurement of protein film thickness using the techniques of ellipsometry and AFM lithography, which shed light onto response of CNT FETs to films of protein.

CHAPTER 6

CONCLUSION

This thesis addressed many issues that are relevant for electrical sensing applications in biological environments. As an experimental platform we have used carbon nanotube field-effect transistors for the detection of biological proteins. Using this experimental platform we have probed many of properties that control sensor function, such as surface potentials, the response of field effect transistors to absorbed material, and the mass transport of proteins. Field effect transistor biosensors are a topic of active research, and were first demonstrated in 1962. Despite decades of research, the mass transport of proteins onto a sensor surface has not been quantified experimentally until now. Protein transport is an important issue because signals from low analyte concentrations can take hours to develop. Guided by mass transport modeling we modified our sensors to demonstrate a 2.5 fold improvement in sensor response time. It is easy to imagine a 25 fold improvement in sensor response time using more advanced existing fabrication techniques. This improvement would allow for the detection of low concentrations of analyte on the order of minutes instead of hours, and will open the door point-of-care biosensors.

(1) Lutz, A. M.; Willmann, J. K.; Cochran, F. V.; Ray, P.; Gambhir, S. S. *PLoS Med* **2008**, *5*, e170.
(2) Petricoin, E. F.; Hackett, J. L.; Lesko, L. J.; Puri, R. K.; Gutman, S. I.; Chumakov, K.; Woodcock, J.; Feigal, D. W.; Zoon, K. C.; Sistare, F. D. *Nat Genet*.
(3) Johnsson, B.; Löfås, S.; Lindquist, G. *Anal. Biochem* **1991**, *198*, 268-277.
(4) Dürkop, T.; Getty, S. A.; Cobas, E.; Fuhrer, M. S. *Nano Letters* **2004**, *4*, 35-39.
(5) Rinkiö, M.; Johansson, A.; Paraoanu, G. S.; Törmä, P. *Nano Letters* **2009**, *9*, 643-647.
(6) Stern, E.; Vacic, A.; Rajan, N. K.; Criscione, J. M.; Park, J.; Ilic, B. R.; Mooney, D. J.; Reed, M. A.; Fahmy, T. M. *Nat Nano* **2010**, *5*, 138-142.
(7) Rich, R. L.; Myszka, D. G. *J. Mol. Recognit.* **2005**, *18*, 431-478.
(8) Wanekaya, A. K.; Chen, W.; Myung, N. V.; Mulchandani, A. *Electroanalysis* **2006**, *18*, 533-550.
(9) Baselt, D. R.; Lee, G. U.; Natesan, M.; Metzger, S. W.; Sheehan, P. E.; Colton, R. J. *Biosensors and Bioelectronics* **1998**, *13*, 731-739.
(10) Mohanty, N.; Berry, V. *Nano Letters* **2008**, *8*, 4469-4476.
(11) Allen, B. L.; Kichambare, P. D.; Star, A. *Adv. Mater.* **2007**, *19*, 1439-1451.
(12) Saphire, E. O.; Parren, P. W. H. I.; Pantophlet, R.; Zwick, M. B.; Morris, G. M.; Rudd, P. M.; Dwek, R. A.; Stanfield, R. L.; Burton, D. R.; Wilson, I. A. *Science* **2001**, *293*, 1155 - 1159.
(13) Ellington, A.; Szostak, J. *Nature* **1990**, *346*, 818-822.
(14) Tuerk, C.; Gold, L. *Science* **1990**, *249*, 505 -510.
(15) Tombelli, S.; Minunni, M.; Mascini, M. *Biosensors and Bioelectronics* **2005**, *20*, 2424-2434.
(16) Zhou, T.; Xu, L.; Dey, B.; Hessell, A. J.; Van Ryk, D.; Xiang, S.-H.; Yang, X.; Zhang, M.-Y.; Zwick, M. B.; Arthos, J.; Burton, D. R.; Dimitrov, D. S.; Sodroski, J.; Wyatt, R.; Nabel, G. J.; Kwong, P. D. *Nature* **2007**, *445*, 732-737.
(17) Ingle, J. D.; Crouch, S. R. *Spectrochemical Analysis*; Prentice Hall: Englewood Cliffs, 1988.
(18) Moerner, W. E.; Fromm, D. P. *Rev. Sci. Instrum.* **2003**, *74*, 3597.
(19) Besteman, K.; Lee, J.-O.; Wiertz, F. G. M.; Heering, H. A.; Dekker, C. *Nano Letters* **2003**, *3*, 727-730.
(20) Chen, R. J. *Proceedings of the National Academy of Sciences* **2003**, *100*, 4984-4989.
(21) Kauffman, D. R.; Star, A. *Chem. Soc. Rev.* **2008**, *37*, 1197.
(22) Cui, Y.; Wei, Q.; Park, H.; Lieber, C. M. *Science* **2001**, *293*, 1289-1292.
(23) Stern, E.; Klemic, J. F.; Routenberg, D. A.; Wyrembak, P. N.; Turner-Evans, D. B.; Hamilton, A. D.; LaVan, D. A.; Fahmy, T. M.; Reed, M. A. *Nature* **2007**, *445*, 519-522.
(24) Dong, X.; Shi, Y.; Huang, W.; Chen, P.; Li, L.-J. *Adv. Mater.* **2010**, *22*, 1649-1653.
(25) Zheng, G.; Patolsky, F.; Cui, Y.; Wang, W. U.; Lieber, C. M. *Nat Biotech* **2005**, *23*, 1294-1301.
(26) Maehashi, K.; Katsura, T.; Kerman, K.; Takamura, Y.; Matsumoto, K.; Tamiya, E. *Analytical Chemistry* **2007**, *79*, 782-787.

(27) Stern, E.; Wagner, R.; Sigworth, F. J.; Breaker, R.; Fahmy, T. M.; Reed, M. A. *Nano Letters* **2007**, *7*, 3405-3409.
(28) Tu, X.; Manohar, S.; Jagota, A.; Zheng, M. *Nature* **2009**, *460*, 250-253.
(29) Kukovitsky, E. F.; L'vov, S. G.; Sainov, N. A.; Shustov, V. A.; Chernozatonskii, L. A. *Chemical Physics Letters* **2002**, *355*, 497-503.
(30) Iijima, S. *Nature* **1991**, *354*, 56-58.
(31) Li, F.; Cheng, H. M.; Bai, S.; Su, G.; Dresselhaus, M. S. *Appl. Phys. Lett.* **2000**, *77*, 3161.
(32) Walters, D. A.; Ericson, L. M.; Casavant, M. J.; Liu, J.; Colbert, D. T.; Smith, K. A.; Smalley, R. E. *Appl. Phys. Lett.* **1999**, *74*, 3803.
(33) Bolotin, K. I.; Sikes, K. J.; Jiang, Z.; Klima, M.; Fudenberg, G.; Hone, J.; Kim, P.; Stormer, H. L. *Solid State Communications* **2008**, *146*, 351-355.
(34) Guo, T.; Nikolaev, P.; Rinzler, A. G.; Tomanek, D.; Colbert, D. T.; Smalley, R. E. *The Journal of Physical Chemistry* **1995**, *99*, 10694-10697.
(35) José-Yacamán, M.; Miki-Yoshida, M.; Rendón, L.; Santiesteban, J. G. *Appl. Phys. Lett.* **1993**, *62*, 657.
(36) Artyukhin, A. B.; Stadermann, M.; Friddle, R. W.; Stroeve, P.; Bakajin, O.; Noy, A. *Nano Letters* **2006**, *6*, 2080-2085.
(37) Heller, I.; Janssens, A. M.; Mannik, J.; Minot, E. D.; Lemay, S. G.; Dekker, C. *Nano Letters* **2008**, *8*, 591-595.
(38) Abe, M.; Murata, K.; Kojima, A.; Ifuku, Y.; Shimizu, M.; Ataka, T.; Matsumoto, K. *The Journal of Physical Chemistry C* **2007**, *111*, 8667-8670.
(39) So, H.-M.; Won, K.; Kim, Y. H.; Kim, B.-K.; Ryu, B. H.; Na, P. S.; Kim, H.; Lee, J.-O. *Journal of the American Chemical Society* **2005**, *127*, 11906-11907.
(40) Morgan, C.; Newman, D.; Price, C. *Clin Chem* **1996**, *42*, 193-209.
(41) Sheehan, P. E.; Whitman, L. J. *Nano Letters* **2005**, *5*, 803-807.
(42) Squires, T. M.; Messinger, R. J.; Manalis, S. R. *Nat Biotech* **2008**, *26*, 417-426.
(43) Charlier, J.-C.; Blase, X.; Roche, S. *Rev. Mod. Phys.* **2007**, *79*, 677.
(44) Bard, A. J.; Faulkner, L. *ELECTROCHEMICAL METHODS fundamentals and applications*; John Wiley & Sons.
(45) Bockris, J. O.; Reddy, A. K. N. *Modern Electrochemistry 1: Ionics, 2nd Edition*; 2nd ed.; Springer, 1998.
(46) McEuen, P. L.; Fuhrer, M. S.; Hongkun Park *Nanotechnology, IEEE Transactions on* **2002**, *1*, 78-85.
(47) Zhou, X.; Park, J.-Y.; Huang, S.; Liu, J.; McEuen, P. L. *Phys. Rev. Lett.* **2005**, *95*, 146805.
(48) Cui, X.; Freitag, M.; Martel, R.; Brus, L.; Avouris, P. *Nano Letters* **2003**, *3*, 783-787.
(49) Zhang, Y.; Dai, H. *Appl. Phys. Lett.* **2000**, *77*, 3015.
(50) Rosenblatt, S.; Yaish, Y.; Park, J.; Gore, J.; Sazonova, V.; McEuen, P. L. *Nano Letters* **2002**, *2*, 869-872.
(51) Kong, J.; Soh, H. T.; Cassell, A. M.; Quate, C. F.; Dai, H. *Nature* **1998**, *395*, 878-881.
(52) Kang, S. J.; Kocabas, C.; Ozel, T.; Shim, M.; Pimparkar, N.; Alam, M. A.; Rotkin, S. V.; Rogers, J. A. *Nat Nano* **2007**, *2*, 230-236.

(53) Wang, C.; Zhang, J.; Ryu, K.; Badmaev, A.; De Arco, L. G.; Zhou, C. *Nano Letters* **2009**, *9*, 4285-4291.
(54) Ding, L.; Tselev, A.; Wang, J.; Yuan, D.; Chu, H.; McNicholas, T. P.; Li, Y.; Liu, J. *Nano Letters* **2009**, *9*, 800-805.
(55) Ducati, C.; Alexandrou, I.; Chhowalla, M.; Amaratunga, G. A. J.; Robertson, J. *J. Appl. Phys.* **2002**, *92*, 3299.
(56) Hur, S.-H.; Park, O. O.; Rogers, J. A. *Appl. Phys. Lett.* **2005**, *86*, 243502.
(57) Jiao, L.; Fan, B.; Xian, X.; Wu, Z.; Zhang, J.; Liu, Z. *Journal of the American Chemical Society* **2008**, *130*, 12612-12613.
(58) Bachtold, A.; Fuhrer, M. S.; Plyasunov, S.; Forero, M.; Anderson, E. H.; Zettl, A.; McEuen, P. L. *Phys. Rev. Lett.* **2000**, *84*, 6082.
(59) Yang, R.; Jin, J.; Chen, Y.; Shao, N.; Kang, H.; Xiao, Z.; Tang, Z.; Wu, Y.; Zhu, Z.; Tan, W. *Journal of the American Chemical Society* **2008**, *130*, 8351-8358.
(60) Zhu, J.; Brink, M.; McEuen, P. L. *Nano Letters* **2008**, *8*, 2399-2404.
(61) Ishigami, M.; Chen, J. H.; Cullen, W. G.; Fuhrer, M. S.; Williams, E. D. *Nano Letters* **2007**, *7*, 1643-1648.
(62) Decher, G. *Science* **1997**, *277*, 1232 -1237.
(63) Duffy, D. C.; McDonald, J. C.; Schueller, O. J. A.; Whitesides, G. M. *Analytical Chemistry* **1998**, *70*, 4974-4984.
(64) Minot, E. D.; Janssens, A. M.; Heller, I.; Heering, H. A.; Dekker, C.; Lemay, S. G. *Appl. Phys. Lett.* **2007**, *91*, 093507.
(65) Mukhopadhyay, R. *Analytical Chemistry* **2007**, *79*, 3248-3253.
(66) Marie, R.; Beech, J. P.; Vörös, J.; Tegenfeldt, J. O.; Höök, F. *Langmuir* **2006**, *22*, 10103-10108.
(67) Vickers, J. A.; Caulum, M. M.; Henry, C. S. *Analytical Chemistry* **2006**, *78*, 7446-7452.
(68) Bourlon, B.; Wong, J.; Miko, C.; Forro, L.; Bockrath, M. *Nat Nano* **2007**, *2*, 104-107.
(69) van Hal, R. E. G.; Eijkel, J. C. T.; Bergveld, P. *Sensors and Actuators B: Chemical* **1995**, *24*, 201-205.
(70) Patolsky, F.; Zheng, G.; Lieber, C. M. *Analytical Chemistry* **2006**, *78*, 4260-4269.
(71) Heller, I.; Männik, J.; Lemay, S. G.; Dekker, C. *Nano Letters* **2009**, *9*, 377-382.
(72) Rodriguez-Maldonado, L.; Fernandez-Nieves, A.; Fernandez-Barbero, A. *Colloids and Surfaces A: Physicochemical and Engineering Aspects* **2005**, *270-271*, 335-339.
(73) Sapsford, K. E.; Ligler, F. S. *Biosensors and Bioelectronics* **2004**, *19*, 1045-1055.
(74) Tombler, T. W.; Zhou, C.; Alexseyev, L.; Kong, J.; Dai, H.; Liu, L.; Jayanthi, C. S.; Tang, M.; Wu, S.-Y. *Nature* **2000**, *405*, 769-772.
(75) Kong, J.; LeRoy, B. J.; Lemay, S. G.; Dekker, C. *Appl. Phys. Lett.* **2005**, *86*, 112106.
(76) Meyers, R. *Encyclopedia of Analytical Chemistry*; John Wiley & Sons Ltd, 2000., 4848–4871
(77) Ellington Lab Aptamer Database. http://aptamer.icmb.utexas.edu/
(78) Chen, R. J.; Zhang, Y.; Wang, D.; Dai, H. *Journal of the American Chemical Society* **2001**, *123*, 3838-3839.
(79) Cui, R.; Widlund, H. R.; Feige, E.; Lin, J. Y.; Wilensky, D. L.; Igras, V. E.; D'Orazio, J.; Fung, C. Y.; Schanbacher, C. F.; Granter, S. R.; Fisher, D. E. *Cell* **2007**, *128*, 853-864.

(80) Green, N. M. Academic Press, 1975; Vol. Volume 29, pp. 85-133.
(81) Waldrep, J. C.; Noe, R. L.; Stulting, R. D. *Investigative Ophthalmology & Visual Science* **1988**, *29*, 1538 -1543.
(82) Tang, X.; Bansaruntip, S.; Nakayama, N.; Yenilmez, E.; Chang, Y.-lan; Wang, Q. *Nano Letters* **2006**, *6*, 1632-1636.
(83) Star, A.; Tu, E.; Niemann, J.; Gabriel, J.-C. P.; Joiner, C. S.; Valcke, C. *Proceedings of the National Academy of Sciences of the United States of America* **2006**, *103*, 921 -926.
(84) De Feijter, J. A.; Benjamins, J.; Veer, F. A. *Biopolymers* **1978**, *17*, 1759-1772.
(85) Noll, F.; Lutsch, G.; Bielka, H. *Immunology Letters* **1982**, *4*, 117-123.